Seismicity, structure and rheology of the lithosphere in the Lake Baikal region

Brian Emmerson, James Jackson, Dan McKenzie and Keith Priestley

Bullard Laboratories, Madingley Road, Cambridge, CB3 0EZ, *UK. E-mail: emmerson@esc.cam.ac.uk*

SUMMARY

This paper combines observations of seismicity, gravity, topography and thermal and velocity structures to investigate the rheological properties of the lithosphere in the Lake Baikal region. We examine the seismogenic thickness (T_s) using 25 earthquakes of M_w 5.1–7.1, whose full source parameters have been determined by inversion of teleseismic waveforms, 13 of which are presented here for the first time. These 25 events, plus six others (M_w 5.0–5.8) whose depths are well constrained, show that moderate earthquakes occur at depths up to ∼30 km in the northeast Baikal rift. Based on the teleseismic waveform modelling results and published relocations of microearthquakes using regional networks, we conclude that the mantle is not a significant source of seismicity in the Baikal region. Using the admittance between free-air gravity and topography, we estimate the effective elastic thickness (T_e) in the region to be between 5 and 20 km. Nowhere do the data require that $T_e > T_s$, consistent with the simple interpretation that the long-term strength of the lithosphere resides in its seismogenic layer. A weak mantle in the Baikal region can be explained by its high temperature, which we estimate by combining local geotherm estimates with the regional upper mantle velocity structure, obtained from fundamental and higher-mode surface waves. Geotherms are fitted to pressure and temperature estimates from mantle nodules at four sites, both within and outside the Siberian shield. In order to constrain the temperatures at the Moho, we estimated crustal thicknesses using teleseismic receiver functions. Moho temperatures are estimated to exceed ∼550°C beneath the Siberian shield and are higher in the more recently deformed mountain belts to the south. Based on a reassessment of oceanic geotherms and seismicity, it seems likely, therefore, that the mantle in the Baikal region is too hot to be a source of long-term strength. This is consistent with the recent suggestion that the distribution of mantle seismicity in both the oceans *and* the continents is dependent on temperature alone. Finally, we note that results from *S*-wave tomography studies, combined with the observed locations of rift-related earthquakes, lead us to suspect that the frequently published position of the edge to the Siberian shield at the surface provides a poor description of that same boundary at depth.

Key words: Baikal, crustal structure, gravity, lithosphere, rheology, seismicity, temperature.

GJI Seismology

1 INTRODUCTION

The rheological properties of the lithosphere must have a fundamental influence on its tectonics and dynamic behaviour. Those properties are likely to be related to lithosphere composition and thermal structure, and their most obvious manifestation is in the distribution of earthquakes and the support of loads. These topics have been controversial in recent years, resulting largely from close re-examination and reinterpretation of earthquake and gravity data (McKenzie & Fairhead 1997; Maggi *et al.* 2000a,b; McKenzie 2003). Two general conclusions arise from this recent history:

(i) The joint interpretation of earthquake, gravity, thermal and compositional data provides more powerful constraints on litho-

sphere rheology than any single source of such information, which, when considered alone, can be ambiguous. For example, the relation between gravity and topography yields an estimate of effective elastic thickness, but not the depth at which that elastic behaviour resides. Earthquakes alone can be interpreted as evidence of significant elastic strain accumulation and release, or simply as manifestations of changing frictional properties. As Maggi *et al.* (2000a) and McKenzie *et al.* (2005) point out, trying to simultaneously reconcile the combination of such observations severely restricts acceptable interpretations of lithospheric strength;

(ii) The comparison between oceanic and continental lithosphere is instructive. For example, if the properties of the mantle part of the lithosphere are different under continents and oceans, it is a

valid and informative question to ask why that should be the case (e.g. McKenzie *et al.* 2005).

If we are to observe patterns and contrasts of lithosphere rheology that can be related to geology (e.g. Jackson *et al.* 2004), we need joint studies of seismicity, gravity, topography, thermal structure and velocity structure from more regions around the world. This paper aims to examine one of the regions for which all these data are available. We first briefly review the current situation.

In most continental settings, earthquakes are restricted to the upper crust (Chen & Molnar 1983). This observation is usually interpreted as the result of a temperature-dependent transition from friction-dominated seismic slip at shallow depths to deeper aseismic creep processes (Brace & Kohlstedt 1980). However, this pattern is not a global one, as shown by Maggi *et al.* (2000b). They showed that in some areas earthquakes are distributed throughout the thickness of the crust, in particular those associated with Archean and Proterozoic shields, such as in parts of east Africa and north India. Using improved estimates of Moho depths from receiver functions, they also found little evidence that the continental mantle is a significant source of seismicity. This is in contrast to the mantle lithosphere beneath the oceans, in which moderate-sized intraplate earthquakes are known to occur (Wiens & Stein 1983). Maggi *et al.* (2000a) and Jackson (2002) concluded that the seismogenic thickness (T_s) of the continental lithosphere involves the upper crust, or the whole crust, but not, to any significant extent, the mantle.

The relationship between gravity anomalies and topography can be used to estimate the ability of the lithosphere to support elastic stresses over geological timescales. By analysing the wavelengths of gravity anomalies associated with surficial and internal loads, it is possible to evaluate the thickness of a conceptual uniform elastic sheet that supports such loads, known as the effective elastic thickness (T_e). Some early estimates of T_e that exceeded the crustal thicknesses in several continental regions seemingly lent support to the suggestion by Chen & Molnar (1983) that the mantle beneath the continents may be relatively strong. (That suggestion came from the apparent occurrence of rare earthquakes just beneath the continental Moho, in places where Maggi *et al.* (2000b) subsequently argued that those earthquakes were in the lower crust.) However, in a reassessment of the techniques used to estimate T_e, McKenzie & Fairhead (1997) and McKenzie (2003) argue that nowhere on the continents does the value of the effective elastic thickness exceed the crustal thickness. Using revised estimates of elastic thickness based on the analysis of McKenzie & Fairhead (1997), Maggi *et al.* (2000a) argued that T_e tracks T_s, with larger values of T_e found in regions where the seismogenic thickness is also larger. Nowhere did they find that the data requires that T_e is greater than T_s, allowing the simple interpretation that the long-term elastic strength of the continental lithosphere resides in its seismogenic layer. In their analysis, there is no need to invoke the continental mantle as a significant source of long-term strength, either from earthquake or gravity data.

A weak continental mantle lithosphere contrasts with that beneath the oceans. Both the seismogenic and elastic thicknesses of oceanic lithosphere exceed the crustal thickness (Wiens & Stein 1983; Burov & Diament 1995, and references therein), implying that the oceanic mantle is strong. The reason for that contrast is becoming clearer. Maggi *et al.* (2000a) originally attributed the difference to small quantities of water, which might weaken the continental mantle lithosphere, but not the anhydrous oceanic lithosphere. They suggested this because intraplate earthquakes in the oceans were thought to occur in material at temperatures up to $750 \pm 100°C$

(Wiens & Stein 1983; Chen & Molnar 1983), whereas estimates of Moho temperatures in continental shields where the lower crust is seismically active were as low as $400 \pm 100°C$ (e.g. Artemieva & Mooney 2001). The continental mantle beneath such regions was apparently cold enough (by comparison with the oceans) to have earthquakes, but evidently did not; so an effect other than temperature was sought to explain this. However, McKenzie *et al.* (2005) re-examined oceanic and continental geotherms, demonstrating the importance of both revised estimates of radiogenic heat production and the temperature dependence of thermal conductivity when reconciling observations of heat flow with mantle nodule geochemistry on the continents. As a result, their new geotherms show that (*a*) the temperature at the Moho in the continental shields is generally higher than previously thought, and (*b*) that the temperature cut-off for earthquakes in the oceanic lithosphere is approximately $600 \pm 100°C$, rather than $750 \pm 100°C$. They also conclude that, if the mantle is aseismic above $600°C$, this explains the distribution of mantle seismicity everywhere, with no effect other than temperature needed to explain the lack of mantle earthquakes in the continental lithosphere.

The focus of this paper is the Baikal rift system in southeast Siberia, which is a particularly interesting region in the context of the issues discussed above. It lies northeast of the deforming regions in the Tien Shan, Altai and Mongolia, close to the surface expression of the Proterozoic–Palaeozoic suture between the almost aseismic and apparently rigid Siberian shield and the younger Sayan-Baikal fold belt to the southeast (Fig. 1). The contrast between the ancient shields and the younger Phanerozoic orogenic belts is central to the current debates on lithosphere rheology (DeCelles *et al.* 2002; Jackson *et al.* 2004). In the Baikal rift system, the predominant mode of deformation is extension, which is thought to arise either as a far-field effect of the India-Eurasia collision (Molnar & Tapponnier 1975), or as the result of mantle upwelling beneath the rift axis (e.g. Gao *et al.* 1994a,b), or a combination of the two (Petit *et al.* 1998). Several authors (Vertlib 1981, 1997; Déverchère *et al.* 1991, 2001; Radziminovich *et al.* 2003) have reported locally recorded earthquakes in the lower crust and upper mantle along the rift zone. Furthermore, some estimates of effective elastic thickness in the rift zone are as large as 60 km (Ruppel *et al.* 1993), which exceeds all estimates of crustal thickness in the region. If true, both sets of observations suggest that the upper mantle beneath the rift zone is strong, contradicting the pattern found by Maggi *et al.* (2000a). The principal motivation for this study is to re-evaluate estimates of T_s and T_e in the Baikal region using teleseismic earthquake data and more modern analyses of gravity and topography. In addition, we calculate lithosphere geotherms from nodule data in four places, both within and outside the Siberian shield, and compare the temperature structures with the velocity structure obtained from multimode surface wave dispersion. Construction of those geotherms requires estimates of the crustal thickness, which we obtain from both published and new receiver function inversions (Fig. 1). We are then able to compare mechanical properties (T_e, T_s) with lithosphere composition and structure.

We begin with an assessment of seismogenic thickness based on both published and new teleseismic data, in which we present the full source parameters for 25 (M_w 5.1–7.1) earthquakes, obtained from waveform modelling. We then compare these data with published studies of locally recorded events. Next, we reassess the effective elastic thickness using the admittance between topography and free-air gravity. Following this, we present receiver function analyses from three sites on the Siberian shield, which are then used, together with pressure and temperature estimates from nodules, to
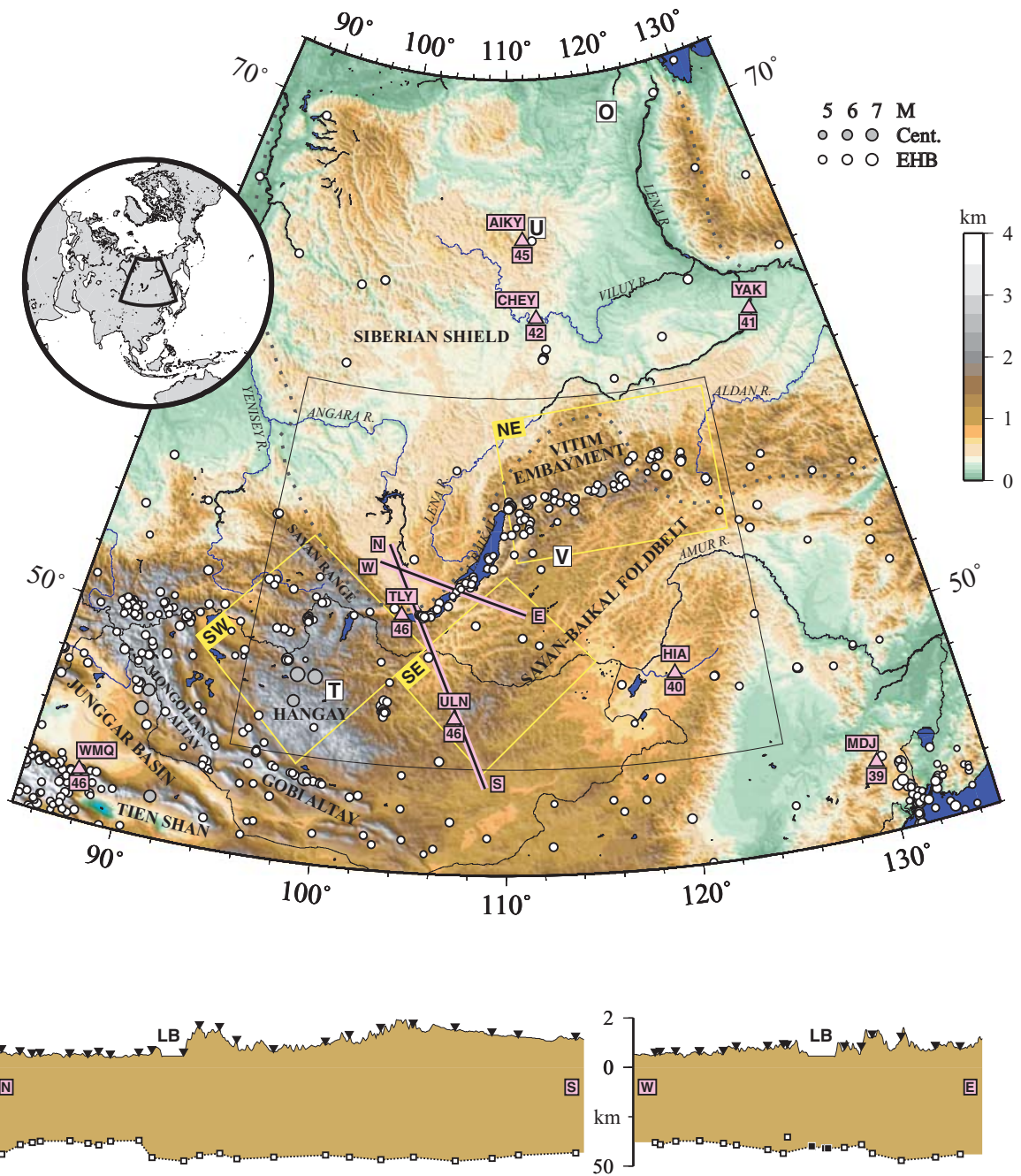
Figure 1. Topography, major tectonic features, regional seismicity, and crustal thickness estimates from northeast Asia. The approximate geologically mapped boundary of the relatively flat Siberian shield is shown as a dotted line (after Goodwin 1991). White dots are epicentres from 1964–2002, taken from the updated catalogue of Engdahl *et al.* (1998), referred to as the EHB catalogue. Grey dots represent earthquakes from 1900–1963 with magnitude ≥7, listed in the centennial catalogue of Engdahl & Villaseñor (2002). All epicentre symbols are scaled according to the inset magnitude scale. A narrow band of seismicity roughly parallel to Lake Baikal delineates the position of the rift zone, and does not follow the geological estimate of the Siberian shield boundary (dotted line) between ∼110°–120°E. Profiles along lines NS and WE are presented below, showing Moho depths determined from teleseismic receiver functions (Gao *et al.* 2004, white squares) and a joint wide-angle/multichannel seismic reflection profile (ten Brink & Taylor 2002, black squares). Lake Baikal is labelled as LB on each profile. Permanent GDSN and temporary Geofon broad-band stations are shown on the map as light pink triangles. Below each station we show crustal thickness estimates (in km), determined using receiver functions by Mangino *et al.* (1999, stations HIA, MDJ and WMQ), Gao *et al.* (2004, stations TLY and ULN, both contained within profile NS) and this study (Section 4, stations AIKY, CHEY and YAK). The black line contains the area detailed in Fig. 2. Yellow boxes labelled SW, SE and NE respectively indicate the southwest Baikal, southeast Baikal and northeast rift regions (Figs 4a–c) used in spectral estimates of the effective elastic thickness (*Te*, Section 3). The positions of nodules used in Figs 9(a), (b), (c) and (d) are shown as letters U, O, V and T respectively.

estimate geotherms at four locations in the region. These geotherms are compared with the velocity structure from surface wave tomography, before combining all of the results in a discussion of how lithosphere mechanical properties are related to composition and thermal structure in the region.

2 SEISMOGENIC THICKNESS T_s

2.1 Data sources

In order to assess the seismogenic thickness T_s of the Baikal rift zone, we need to obtain accurate estimates of earthquake depths. We consider two sources of data: local events recorded by various networks (discussed below) and events recorded teleseismically by permanent global stations.

Several earlier studies (Doser 1991a,b) modelled teleseismic waveforms to estimate source parameters in the region, but there exists over a decade of data yet to be studied in this way. The best quality results we present here are determined by inversion of P and SH waveforms for all source parameters, and are listed for 25 earthquakes of M_w 5.1–7.1 in Table 1. Routinely determined Harvard CMT solutions use low-pass filtered data that is unable to resolve the depths of crustal earthquakes with sufficient accuracy for our

purposes. In some cases, shorter periods were used in the CMT inversion (e.g. Ekström & England 1989) and these depths are included in Table 2. In some other cases, we were able to constrain the source depth by waveform modelling, but fixed the source orientation to that of the long-period Harvard CMT solutions (also in Table 2).

2.2 Teleseismic body-wave modelling

2.2.1 Inversion for all source parameters

Of the 25 solutions presented in Table 1, 13 are from body-wave inversions carried out in this study. The other solutions we have selected, particularly those by Bayasgalan & Jackson (1999) and Bayasgalan *et al.* (2005), were determined using essentially the same algorithm. We take broadband seismograms from the Global Digital Seismograph Network (GDSN) and change the response to that of a WWSSN 15–100 long-period instrument using a deconvolution procedure. For this range of periods, seismic waves are relatively insensitive to complexities in local velocity structure, and an event of M_w 5.0–6.5 can, in principle, be modelled as a point source (the centroid).

We use the MT5 version (Zwick *et al.* 1994) of the algorithm developed by McCaffrey & Abers (1988) and McCaffrey *et al.* (1991),

Table 1. Earthquake source parameters from inversion of teleseismic body-waveforms. Epicentres and origin times from 1964–2004 are from the updated catalogue of Engdahl *et al.* (1998), apart from the 1967 January 5 and 20 Mogod earthquakes (locations are from Bayasgalan & Jackson 1999). Moment magnitude is given by $M_w = \frac{2}{3}\log_{10} M_0 - 6.03$, where M_0 is the scalar moment in Nm. Strikes, dips and rakes of the two nodal planes are s1, d1, r1 and s2, d2 and r2, and z is the determined centroid depth. An entry is flagged 'm' if it is modelled as a multiple event. Mechanisms and focal depths for such entries are listed for the first sub-event only, whereas M_w is based on the total moment released by all events in the sequence. The final column refers to the work in which the inversion is published. Where more than one solution is available, we have used the last entry listed here. Da and Db refer to work by Doser (1991a,b); DL is from Delouis *et al.* (2002); H is Huang & Chen (1986); BJ is Bayasgalan & Jackson (1999); B is Bayasgalan *et al.* (2005); BN is Brazier & Nyblade (2003). A is the Appendix of this paper. All of these focal mechanisms are plotted in Fig. 2 with black ($z < 20$ km) or red ($z \geq 20$ km) compressional quadrants.

Earthquake source parameters for the Baikal region, determined by body-wave modelling

Date			Time	Lat./°	Lon./°	M_w	s1	d1	r1	s2	d2	r2	m	z/km	Ref.
1917	4	29	115530	56.17	114.62	6.6	340	70	−16	76	75	−159	.	16	Db
1950	4	4	184410	51.70	101.00	6.9	100	75	0	10	90	165	.	14	Da,DL
1957	6	27	000935	56.39	116.39	7.1	100	81	−25	194	65	−170	m	10	Db
1958	1	5	113044	56.51	121.11	5.8	257	50	−100	92	41	−78	m	8	Db
1958	9	14	142137	56.61	121.00	6.2	63	63	−75	212	31	−117	.	6	Db
1959	8	29	170314	52.64	106.90	6.2	248	53	−50	14	52	−130	.	14	Da
1962	11	11	113140	55.84	113.22	5.7	215	58	−78	13	34	−108	.	5	Db
1967	1	5	001440	48.28	103.05	7.0	2	83	−179	272	89	−7	m	5	H,BJ
1967	1	18	053435	56.65	121.00	5.5	63	57	−117	286	42	−55	.	10	Db
1967	1	20	015720	48.23	103.14	6.4	319	42	102	123	49	79	.	8	H,BJ
1989	4	20	225956	57.17	122.10	6.2	114	71	45	6	48	154	.	29	Db,A
1989	5	13	033501	50.16	105.42	5.5	210	87	164	301	74	3	.	8	B
1989	5	17	050438	57.08	122.13	5.8	13	62	−165	276	77	−29	.	28	Db,A
1991	12	27	090940	51.07	98.17	6.4	244	72	−15	339	76	−161	.	13	B
1994	4	26	185929	56.74	117.97	5.4	81	24	−56	225	70	−104	.	14	A
1994	8	21	155601	56.74	118.01	5.9	46	44	−99	238	47	−81	.	12	A
1995	6	29	230230	51.91	103.19	5.7	73	41	−40	195	65	−124	.	16	B,A
1998	9	24	185341	46.26	106.34	5.5	97	76	9	5	81	166	.	27	A
1999	3	21	161603	55.93	110.31	5.7	267	22	−74	70	69	−96	.	3	BN,A
1999	3	21	161706	55.99	110.29	5.8	222	20	−113	66	72	−82	.	3	A
1999	5	30	155647	55.85	110.13	5.2	198	40	−108	41	52	−75	.	6	A
1999	9	8	023853	57.49	120.25	5.1	266	46	−111	115	48	−70	.	6	A
1999	12	21	110049	55.84	110.14	5.4	42	59	−97	235	32	−79	.	5	A
2003	9	16	112454	56.06	111.37	5.5	38	40	−111	245	53	−73	.	15	A
2005	11	10	192956	57.44	120.50	5.8	96	52	−77	255	40	−106	.	7	A

Table 2. Fault plane solutions from the Harvard CMT catalogue, excluding those events already listed in Table 1. Epicentres and origin times up to the end of 2004 are from the updated catalogue of Engdahl *et al.* (1998), with the exception of event 870221 (ISC location). The moment magnitude M_w is calculated as in Table 1 and the strikes, dips and rakes of the two nodal planes are s1, d1, r1, and s2, d2 and r2. Depths (z) of shallow earthquakes are not reliably determined by the routine Harvard CMT procedure and so are omitted here, unless we have some other way of measuring the depth. An A in the final column indicates that we have been able to improve our estimate of the source depth, either by restricting our modelling of long-period waveforms to an inversion for just three source parameters (the source time function, depth and moment), or by forward modelling the recordings of first arrivals and their associated free surface reflections on vertical component broadband seismograms (see text and Appendix for details). Both of these methods use the Harvard CMT best double-couple source orientation. The percentage double-couple (γ) of the CMT solutions is defined as $\gamma = (1 - \frac{3|\lambda_2|}{|\lambda_1|+|\lambda_3|}) \times 100$ per cent, where λ_1, λ_2 and λ_3 are respectively the minimum, intermediate and maximum eigenvalues of the moment tensor. A pure double-couple source (slip on a fault) has $(\lambda_1, \lambda_2, \lambda_3) = (-1, 0, +1)$ and $\gamma = 100$ per cent, whereas a linear vector dipole, $(\lambda_1, \lambda_2, \lambda_3) = (-\frac{1}{2}, -\frac{1}{2}, +1)$, has $\gamma = 0$ per cent. Source parameters from a much broader-band CMT-type inversion by Ekström & England (1989) are denoted by an E in the last column. Aftershocks from the event marked R were relocated using a temporary network and found to be between 5–25 km deep by Radziminovitch *et al.* (2005), who suggest that the main shock nucleated within the crystalline basement. Despite its suitable magnitude, we were unable to model the complex waveforms from this event, which could indicate a complicated rupture history. The strike, dip and rake for the event labelled Q are from the quick CMT catalogue (Ekström 1994), but the depth and moment are from modelling performed by us. All of our modelling results are detailed in the Appendix. Focal mechanisms are plotted in Fig. 2 with dark grey compressional quadrants (for depths z that are either unconstrained, or less than 20 km), or light red ones ($z \geq 20$ km).

Best double-couple Harvard CMT solutions

Date			Time	Lat./°	Lon./°	M_w	s1	d1	r1	s2	d2	r2	γ	z/km	Ref.
1978	8	3	060734	52.12	96.94	5.7	187	53	148	298	65	42	97	14	E
1980	2	10	044604	48.96	121.99	5.1	130	54	6	36	85	144	44	.	
1981	5	22	095122	51.99	105.77	5.4	18	18	−118	227	74	−81	84	.	
1981	5	27	212608	54.01	108.84	5.3	64	23	−96	251	67	−87	57	.	
1981	8	16	175413	50.59	96.83	5.2	166	53	139	284	58	45	58	.	
1987	2	21	221953	54.40	110.33	4.9	176	33	−114	24	60	−75	40	.	
1987	7	7	170730	56.67	121.01	5.3	260	27	−91	81	63	−89	80	.	
1988	12	15	064054	46.52	95.59	5.2	171	84	179	261	89	6	100	.	
1989	4	29	062541	57.16	122.19	5.4	182	73	−177	91	87	−17	81	.	
1989	10	25	202902	57.53	118.88	5.3	68	40	−78	232	51	−100	64	28	A
1990	10	26	181737	56.12	110.16	5.2	215	56	−149	106	65	−38	66	.	
1991	9	12	003333	54.90	111.14	5.0	235	25	−65	28	67	−101	86	22	A
1992	2	14	081827	53.95	108.91	5.3	249	33	−65	40	60	−105	94	15	A
1995	11	13	084316	56.08	114.58	5.8	56	43	−59	197	54	−116	93	21	A
1999	2	25	185831	51.63	104.94	5.9	66	36	−86	241	54	−93	100	.	R
1999	5	27	160125	55.85	110.18	5.1	269	78	−7	0	83	−168	39	.	
1999	5	31	193454	55.82	110.16	5.1	285	27	−69	82	65	−100	43	.	
2000	5	31	162810	51.68	105.02	5.0	247	40	−75	48	52	−102	44	.	
2005	4	27	073616	51.25	98.25	5.3	342	79	−171	250	81	−11	90	11	Q,A
2005	12	11	155415	57.43	120.75	5.7	266	45	−75	65	47	−105	99	.	

which inverts *P* and *SH* waveform data for the source time function, scalar moment, strike, dip, rake and centroid depth. Constraining the source to be a pure double-couple, we model the *P*, *pP* and *sP* phases on vertical component seismograms in the epicentral distance range 30°–90°, and the *S* and *sS* phases on transverse components in the range 30°–80°. Amplitudes are corrected for geometrical spreading and for anelastic attenuation using Futterman operators with a t^* of 1.0 and 4.0 s for *P* and *SH* waves respectively. As Maggi *et al.* (2000b) point out, uncertainties in t^* lead to uncertainties in source duration and scalar moment, but have a small effect on centroid depth and source orientation. The Harvard CMT solution (Dziewonski *et al.* 1981) is used as a starting model for our inversion and synthetic long-period waveforms are aligned with picks from the broadband data wherever possible. Owing in part to a lack of knowledge about source structure, we use a simple half-space with velocities $V_p = 6.5$ km s^{-1}, $V_s = 3.7$ km s^{-1} and density $\rho = 2800$ kg m^{-3}.

As the depth is the source parameter of most interest to us, we performed sensitivity tests to estimate how well our solutions are constrained. Details of all the individual analyses and tests are given in the online Appendix. Typical uncertainties in centroid depths are ±4 km, which is sufficient to show whether the mantle or lower crust are seismically active; the main concern of this paper. Typical uncertainties in the other parameters (such as strike, dip and rake) that describe the best fitting or 'minimum misfit' solutions are discussed elsewhere (e.g. Nábělek 1984; McCaffrey & Nábělek 1987; Molnar & Lyon-Caen 1989; Taymaz *et al.* 1990). Our new solutions, along with those from other authors, are listed in Table 1. Although solutions for events prior to 1960 are recorded by relatively few stations, there is enough information presented in the cited references to confirm the published depths. For example, several different source orientations have been proposed for the M_w 6.9 1950 Mondy earthquake, and these are discussed in further detail by Delouis *et al.* (2002), but enough evidence exists to suggest that the centroid was indeed shallow, even if the source orientation is not well constrained.

2.2.2 Inversion and forward modelling for depth only

When only a few stations with a sparse azimuthal distribution were available, it was not possible to invert long-period waveforms for all source parameters. In such cases, we fixed the strike, dip and rake to

that of the best double-couple Harvard CMT solution and inverted for the source time function, seismic moment and depth. If long-period records for an event were too poor to do this, we attempted to forward-model the vertical component broadband data instead. In these cases, we used the program WKBJ3 (Chapman 1978; Chapman *et al.* 1988), which traces rays through a spherical Earth using the WKBJ approximation for turning rays. Impulse responses for *P*, *pP* and *sP* phases are generated using a version of the AK135 global velocity model (Kennett *et al.* 1995), modified to have a crustal thickness of 40 km. We convolve the impulse responses with the relevant station's broadband response and an attenuation corresponding to $t^* = 1.0$ s. Synthetics and data are aligned at the first peak or trough after the onset of the *P* wave and the depth adjusted to obtain a satisfactory visual fit. This approach is only successful when a surface reflection (*pP* or *sP* phase) can be identified with

some confidence, and we found, in practice, that it worked best for earthquakes with depths of 20 km or more.

2.3 Focal depths and seismogenic thickness, T_s

2.3.1 Teleseismic data

Focal mechanisms and reliable depths for teleseismically located earthquakes are listed in Tables 1 and 2 and shown in Fig. 2. The main pattern revealed by well-constrained centroid depths of moderate-sized earthquakes in Fig. 2 is clear: events deeper than 20 km (red focal spheres) are concentrated in the northeast. To the west of Lake Baikal and beneath the lake itself there are no centroids with depths greater than 16 km. Between 110° and 115°E are two events with depths >20 km (at 21 and 22 km), and east of 115°E are three events
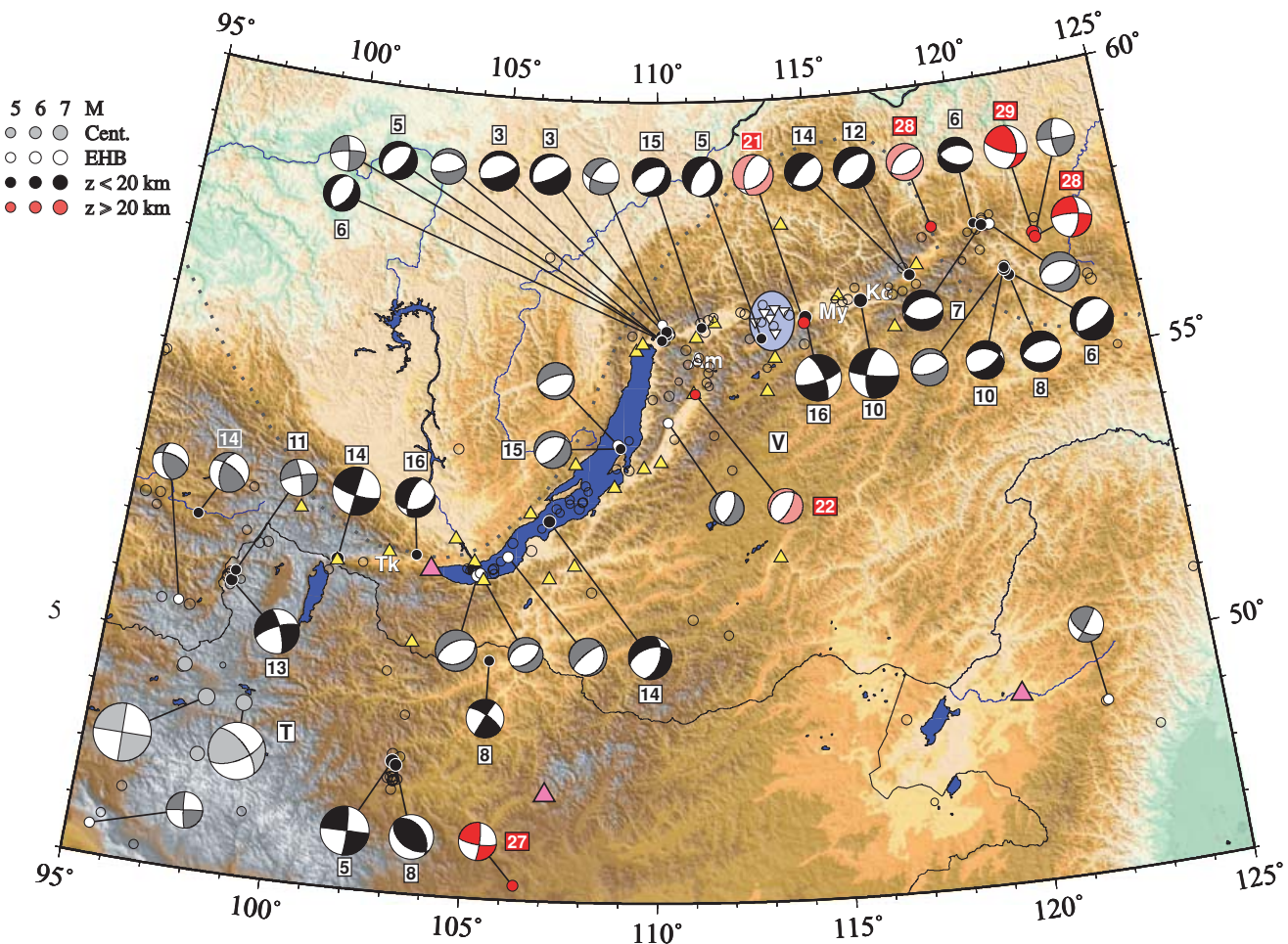

Figure 2. Fault plane solutions in the Baikal region. Focal spheres produced from long-period waveform inversion for all source parameters are plotted with red compressional quadrants if their modelled depth (z) is 20 km or more, and black compressional quadrants if z is less than 20 km (Table 1). We plot best double-couple focal mechanisms from the Harvard CMT catalogue (Table 2) with grey compressional quadrants if they are shallower than 20 km, or if we were unable to confirm their depth, and with light red compressional quadrants if z exceeds 20 km. Reliable depths are labelled alongside the focal spheres. Depths constrained by inversion of long-period waveforms (either for just the source time function, depth and moment, or for all source parameters) are shown in boxes with black outlines; boxes with white outlines contain depths controlled by other reliable means (see text for details). The great Bolnay (M_w 8.2) and Tsetserleg (M_w 8.3) earthquakes of 1905 are shown by light grey focal spheres (after Schlupp 1996). Epicentres for events occurring between 1900–1963 with magnitude ≥7 are plotted as grey circles (from Engdahl & Villaseñor 2002). Apart from events 670105, 670120 (Table 1) and 870221 (Table 2), epicentres for events occurring between 1964–2004 are from the updated catalogue of Engdahl *et al.* (1998), known as the EHB catalogue. The teleseismic data clearly show that recorded events with depths exceeding 20 km are concentrated in the northeast. A single event located in western Mongolia is anomalously deep (27 km) compared to other earthquakes in that region. The local event studies we discuss (Section 2.3.2) used seismic stations from regional and permanent global networks (yellow triangles and pink triangles respectively), as well as a dense local network (light blue ellipse). **Tk** and **My** are the Tunka and Muya rift basins, shown in Fig. 10, and **Kc** and **Am** show the approximate positions of Kalar-Chara and Amut, discussed in the text. All other symbols are as in Fig. 1.

near 30 km depth (at 28 and 29 km). To the southwest of Baikal, in Mongolia, Bayasgalan *et al.* (2005) found that earthquakes were restricted to the upper crust except on the margins of the Junggar basin (west of Fig. 2). A single new earthquake reported here (date: 980924) in central Mongolia is an anomaly to this general pattern, with a depth of 27 km (see Appendix).

Based on deep seismic sounding profiles as far east as ∼120°E (Suvorov *et al.* 2002) and gravity modelling out to ∼114°E (Burov *et al.* 1994; Petit *et al.* 1997), the Moho depth across much of the rift zone is estimated to be about 40 km. Receiver functions along profiles reported by Zorin *et al.* (2002) and Gao *et al.* (2004) indicate that there is a shallower Moho (∼35 km deep) beneath Lake Baikal itself, where crustal thinning may be present. Beyond Lake Baikal, at the northeastern end of the rift where earthquakes are found at 20–30 km depth, we expect the crust to be at least 40 km thick. Assuming this crustal thickness, none of the events whose depths are presented here were located in the mantle.

2.3.2 Local earthquake data

Several studies (Déverchère *et al.* 1991, 1993, 2001; Vertlib 1981, 1997; Radziminovich *et al.* 2003, and references therein) have relocated local events with magnitudes ∼2–5 using regional and local Russian networks across the rift zone (Fig. 2). Most of these studies are concerned with regions in the northeast part of the rift and find that the seismicity there extends to lower-crustal and potentially upper mantle depths. We argue below that, taking into account event magnitudes and the relative quality of these locations, they provide little evidence pointing to the mantle as an important source of seismicity in the Baikal rift zone.

Vertlib (1981) reports fewer than ten events of magnitude <3 between 50–60 km in the Kalar-Chara region of the northeast rift (∼56.5°N, 117°E, indicated by **Kc** in Fig. 2). All of the remainder (∼1400 events) were located shallower than 42 km. The few deep events are likely to be poorly located in depth, owing to the sparse distribution of regional stations, whose minimum spacing exceeds 100 km. With this in mind, we believe these data may confirm that the lower crust is seismically active, but do not unequivocally show the upper mantle to be a significant source of seismic activity.

From a relocation of 74 local events occurring between 1979 and 1980 in the dense Amut swarm (55.5°N, 111.5°E, **Am** in Fig. 2), Déverchère *et al.* (1991) demonstrate that the lower crust in the northeast rift is seismically active. Five events of magnitude 2.2–2.8 were found to be 'probably in the upper mantle', with likely depths between 40 and 50 km. Of the five events, the smallest event-station distance is ∼40 km. Déverchère *et al.* (1991) looked at these five events carefully, showing that variations in velocity model, trial depth and V_p/V_s ratio affected the depth ranges that were acceptable. The minimum depths of these events range from 38 to 43 km, and the maximum from 45 to 63 km. It is possible, therefore, that some of them occurred below the Moho. However, given their small magnitudes, they do not show that the mantle is a significant source of seismicity either.

Déverchère *et al.* (2001), in a study involving relocation of approximately 600 $M_w \sim 2.2$–4.5 events, restricted to those with epicentres within 40 km of regional stations (small yellow triangles, Fig. 2), deduced that T_s across the whole Baikal rift is ∼35–40 km. A single event was located at 52–54 ± 5 km depth, although it is not in their population of 203 best-located events, and is not discussed further. These general results are supported by those of Radziminovich *et al.* (2003), who also located events using regional networks and found $T_s \sim 35$ km beneath central and southwest Lake Baikal. Their summary of hypocentral relocation studies across the whole rift zone also concludes that $T_s \sim 35$ km.

Of the studies cited above, the best locations are likely to be for events relocated in the North Muya region (∼56.1°N, 113.5°E) by Déverchère *et al.* (1993), within the dense local network shown by the blue ellipse in Fig. 2. They found a 30 km-deep cut-off in seismicity for this area.

2.3.3 T_s summary

Teleseismic waveform modelling of moderate-sized earthquakes suggests that seismic activity is spread throughout the upper 30 km of the crust northeast of Lake Baikal, and restricted to the upper 20 km in the rest of the rift zone (Fig. 2). However, hypocentre relocations for smaller events using regional and local networks suggest that the whole crust may be seismogenic everywhere, with the vast majority of hypocentres being shallower than 30 km. It may be that the crust in the northeast is the only part of the rift capable of producing lower-crustal earthquakes of moderate size, possibly because the deepest events there are occurring in a younger, cooler part of the rift, as suggested by Doser & Yarwood (1994). Alternatively, it may be that the high-quality teleseismic database is not sufficiently long to reflect the long-term distribution of earthquakes with $M_w > 5.5$ in the rift zone. Little incontrovertible evidence exists for mantle seismicity in the region. Where possible mantle earthquakes occur, there is some doubt about their precise depths and they have small magnitudes. We have found no earthquakes with $M_w > 5.5$ in the mantle beneath the Baikal rift zone.

3 2-D ADMITTANCE ESTIMATES OF ELASTIC THICKNESS, T_e

We estimated the elastic thickness (T_e) in three regions of the Baikal rift zone from the spectra of topography and free-air gravity, using the 2-D free-air admittance technique of McKenzie & Fairhead (1997) and McKenzie (2003). In all three regions, we find lower T_e values than previous Bouguer coherence analyses have suggested. The admittance $Z(k)$ is defined by

$$\tilde{g}(k) = Z(k)\tilde{e}(k) + \tilde{n}(k),$$

where $\tilde{g}(k)$ and $\tilde{e}(k)$ are respectively the 2-D Fourier transforms of the free-air gravity and topography. The part of the gravity signal not modelled by the $Z(k)\tilde{e}(k)$ term is represented by the term $\tilde{n}(k)$, which represents gravity anomalies that are incoherent with the topography, and whose significance is discussed at length by McKenzie (2003). The 2-D wavenumber of a signal with wavelength λ is $k = \sqrt{k_x^2 + k_y^2} = 2\pi/\lambda$. T_e is estimated using the part of the gravity signal that is coherent with the topography. The free-air coherence at wavenumber k is

$$\gamma_f^2(k) = \frac{\langle \tilde{g}\tilde{e}^* \rangle^2}{\langle \tilde{g}\tilde{g}^* \rangle \langle \tilde{e}\tilde{e}^* \rangle}.$$

Complex conjugates are indicated by asterisks and angle brackets denote averages over a waveband centred on k.

Following the method used by McKenzie (2003), we use a layered crust (Fig. 3) in which loads can be distributed between the free surface, an intracrustal interface at 15 km depth, and the Moho. Loads placed at our chosen Moho depth (40 km) are set to zero for simplicity. By varying the values of T_e and the proportion F_2 of
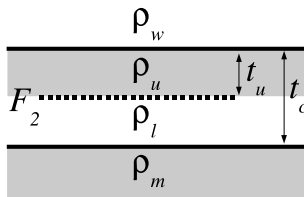
Figure 3. The simple model used to calculate admittance, comprising a two layer crust of thickness t_c (40 km) overlying a mantle half-space (the uppermost layer is water or air, of density ρ_w). Loads can be placed at any of the three interfaces shown, though we set the Moho load to zero. F_2 denotes the proportion of topographically expressed load located at depth t_u (15 km). We assume a linear relationship between gravity and topography. For all three regions studied, densities for the mantle and lower crust are modelled as $\rho_m = 3300$ kg m^{-3} and $\rho_l = 2900$ kg m^{-3} respectively. We set ρ_w to zero. The upper crustal density ρ_u is chosen to best fit the short wavelength admittance in each region. T_e values are calculated assuming a Young's modulus of 95 GPa and a Poisson's ratio of 0.295.

load placed at the intracrustal interface, the misfit H between the observed (Z^o) and calculated (Z^c) admittance is minimized to find the best-fitting elastic thickness, where

$$H(T_e, F_2) = \left[\frac{1}{N} \sum_{n=1}^{N} \left(\frac{Z_n^o - Z_n^c}{\sigma_{Z^o,n}} \right)^2 \right]^{\frac{1}{2}}.$$

The standard deviation of observed admittance values in the nth waveband is $\sigma_{Z^o,n}$. Admittance and coherence estimates are computed for data from N such wavebands.

At short ($\sim$80–110 km) wavelengths, loads are entirely uncompensated and the admittance tends to a constant value ($2\pi G\Delta\rho$) determined by the surface density contrast ($\Delta\rho$). Using this part of the admittance curve, the best-fitting upper crustal density ρ_u is determined for each region. At intermediate wavelengths, the admittance decreases as depression of the Moho reduces the observed gravity signal. We estimate T_e from this change in admittance, using wavelengths up to 300 km. Our admittance measurements at longer wavelengths are less reliable, owing to the small boxes used to sample the gravity and topography data.

The free-air gravity data used to estimate T_e are shown in Figs 4(a)–(c). Data were gridded on a 10×10 km grid before being windowed and filtered using the multitaper technique of McKenzie & Fairhead (1997). To avoid spatial averaging of T_e estimates over dissimilar regions of lithosphere, the Precambrian Siberian shield (Fig. 1)—which lacks a powerful gravity signal over a range of wavenumbers—is not included in the admittance analysis wherever possible. The locations of windowing boxes are restricted further by a lack of suitable gravity data from China, and by the presence of Lake Baikal. We therefore chose three separate sample regions: southwest of Lake Baikal, southeast of Lake Baikal and in the northeast rift (Figs 1 and 4).

Admittance data from the southwest Baikal box of 920×900 km^2 (Figs 1 and 4a) are best fitted using an elastic thickness of 4.8 km, shown as a solid line in Fig. 5(a). In the region where the coherence (Fig. 5b) is high ($\lambda \sim 80$ to 250 km), the fit to the data is good, and we find a well-defined minimum in the misfit H as a function of T_e. This is shown in Fig. 5(d), where the misfit exceeds twice its minimum $H_{\min}$ for values of T_e outside the range 3.8 to 5.8 km. Although the best-fitting internal loading fraction (F_2) is less well defined, it is clear from Fig. 5(c) that the elastic thickness is less than 8 km and likely closer to 5 km. A considerable portion of the southwestern part of this region is contained within a larger region

used by Bayasgalan *et al.* (2005), who employed the same technique to study the elastic thickness of western Mongolia, and found that $T_e < 10$ km. Our results are consistent with theirs and, furthermore, the agreement between the two different areas indicates that the average elastic thickness remains small right up to the edge of the Siberian shield.

In the southeast Baikal region (800×690 km^2, Figs 1 and 4b), the coherence of the gravity signal decreases more rapidly with increasing wavelength (Fig. 6b). Consequently, we estimate T_e by fitting the admittance data (Fig. 6a) for a more restricted range of wavelengths ($80 < \lambda < 170$ km), finding a best fitting value for T_e of 5.2 km. Formally, the misfit (Fig. 6d) exceeds twice its minimum value when T_e is outside the range 4.0–6.4 km, though the trade-off with F_2 shown in Fig. 6c suggests that T_e, though smaller than 10 km, is less well defined than this.

In the northeastern rift zone (890×610 km^2, Figs 1 and 4c), we find a best-fitting elastic thickness of 10.0 km by fitting the admittance (Fig. 7a) at wavelengths up to 300 km. This slightly larger value of T_e is due in part to the presence of the Siberian shield ($T_e \sim 15$ km, after McKenzie 2003), which is certainly contained within part of the northeastern box, and may underlie more of it, depending on the extent to which younger material has been thrust on top of the ancient shield. For the minimum misfit value of F_2, Fig. 7(d) shows that $H > 2H_{\min}$ if T_e lies outside the range 7.6–13.4 km, whereas the contoured misfit (Fig. 7c) indicates that $H > 2H_{\min}$ for T_e outside the range 5 to 18 km, whatever the value of F_2. Clearly the elastic thickness of the northeastern rift zone is less than 18 km, and probably closer to 10 km.

Use of this technique to estimate T_e is sometimes regarded as controversial, owing to the sensitivity of admittance functions to subsurface loading (Forsyth 1985; Pérez-Gussinyé *et al.* 2004). Forsyth (1985) argues that T_e is more reliably determined from the Bouguer coherence, because it is far less sensitive to variations in internal loading. Many authors (e.g. Diament & Kogan 1990; Ruppel *et al.* 1993; Ebinger & Hayward 1996; Simons *et al.* 2000) have adopted his method for this reason. It is important to distinguish between two types of subsurface load: internal loads that lack a topographic signal, and internal loads that are expressed topographically. In the presence of the former, Bouguer coherence techniques can overestimate T_e. These Bouguer techniques assume statistical independence between surficial and internal loads to estimate T_e. This assumption implicitly neglects the presence of internal loads having no topographic expression, which *must* correlate with surficial loads in order to produce flat topography (McKenzie 2003). Such subsurface loads reduce the coherence between gravity and topography, and cannot be represented by the internal loading fraction F_2. On the other hand, F_2 *can* be used to represent subsurface loads that *are* expressed topographically. We estimate the value of F_2 using the same simple model as McKenzie (2003), where the arguments summarized here are presented in more detail. Whatever the source of internal loading, part of the free-air gravity signal must correlate with the topography, since the topography always produces a gravity signal. By using wavebands for which the free-air coherence (eq. 3) is high, we reduce the effect loads without topographic expression have on our estimates of elastic thickness.

We are restricted by the gravity data set and regional geography to boxes of dimensions that are small compared to the those often used in spectral estimates of T_e. It is possible that our admittance estimates are distorted slightly by spectral leakage (sections 2 and 3 of Pérez-Gussinyé *et al.* 2004). However, given that in the areas sampled there is little power in the gravity signal at wavelengths exceeding $\sim$300 km (Fig. 4), it is not likely that such distortions
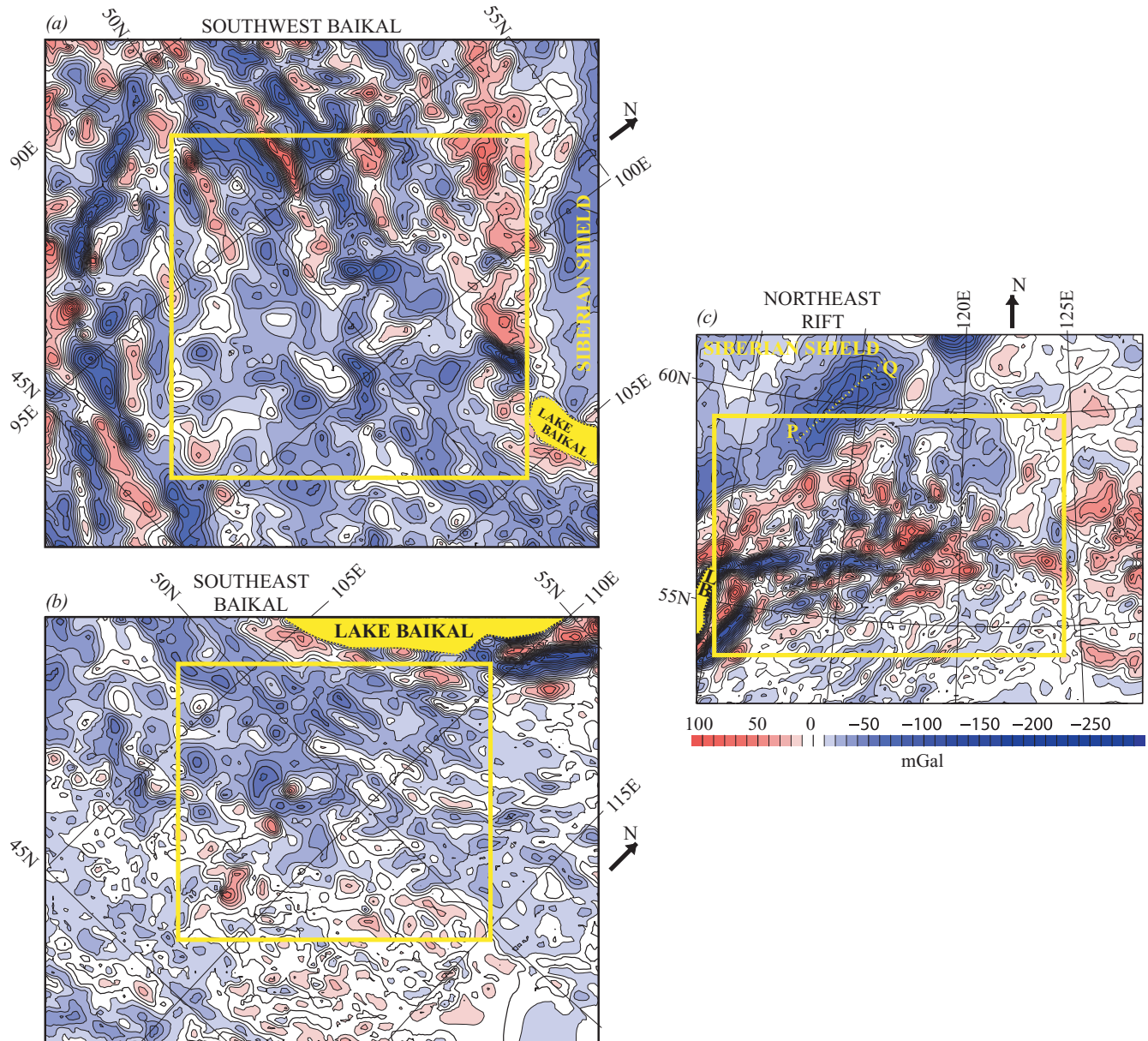
Figure 4. Free-air gravity anomalies (mGal) of the Baikal region. Gravity data were kindly made available by Derek Fairhead of GETECH. Yellow shading shows the approximate position of Lake Baikal. The edge to the low-energy gravity signal of the relatively flat Siberian shield can be seen along the right hand border of Fig. (a), as far southeast as Lake Baikal. Yellow rectangles in figures (a), (b) and (c) show respectively the locations of boxes used for the admittance analysis in Figs 5 (southwest Baikal), 6 (southeast Baikal) and 7 (northeast rift). Box locations are also shown in Fig. 1. The projection used in the analysis of the southwest and southeast boxes was a transverse Mercator with the pole at 55°N, 15°E; the northeast box data were projected in the same way, using a pole at 0°N, 32°E. Line PQ bisects a portion of the negative free-air gravity anomaly discussed in Sections 5.2 and 6.

cause our T_e estimates to differ significantly from the true values. Tests with synthetic data show that, for boxes of the size we are limited to consider here, the difference between the true T_e and the value retrieved using the free-air admittance is typically ∼4 km for a theoretical T_e of 5 km, and ∼6 km for a value of 10 km (Crosby 2006). Conversely, caution should be taken in interpreting the value of F_2, which is poorly constrained as a consequence of both its sensitivity to the shape of the admittance function at intermediate wavelengths, and to the depth of internal loading assumed in the model.

Two studies have used the Bouguer coherence technique of Forsyth (1985) to estimate the effective elastic thickness of the

Baikal rift zone, each finding a higher value than we have here. Diament & Kogan (1990) estimate T_e ∼ 30 km, using coherence data from an area of 1570 × 1570 km², which is much larger than the boxes examined here, and encompasses Lake Baikal and a large area of the Siberian shield. In a study of a similar region using a higher resolution data set, Ruppel *et al.* (1993) find T_e values in the range 40–60 km. As argued by McKenzie (2003) and summarized above, these estimates can only provide an upper bound on the elastic thickness. van der Beek (1997) applied various rifting models to the Baikal region and found, by comparing topography and Bouguer anomalies with modelled values, that 'best-fit elastic thicknesses are in the range 30–50 km'. However, the misfits as a
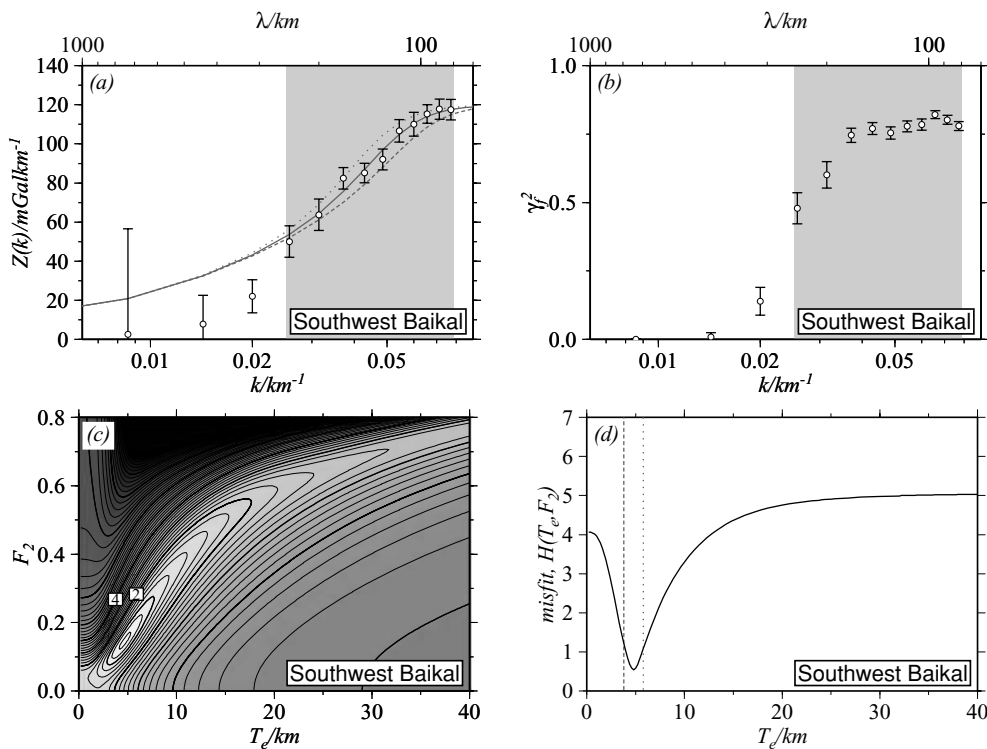
Figure 5. Free-air admittance (*a*) and coherence (*b*) measurements from the southwest Baikal box (Fig. 4). We chose an upper crustal density ρ_u of 2860 kg m^{-3} to best fit the admittance between $80 < \lambda_{\rho_u} < 100$ km, before fitting the admittance to wavelengths $80 < \lambda_Z < 250$ km (shaded in a and b). (c) Contours of the misfit H (eq. 3) between the calculated and observed admittance as a function of elastic thickness T_e and the fraction of internal load F_2. There is a well-defined minimum in the misfit surface at $T_e = 4.8$ km, $F_2 = 0.15$. (d) Misfit as a function of T_e for the best-fitting value of F_2 (0.15), with a clear minimum at $T_e = 4.8$ km. The solid line in (a) corresponds to this elastic thickness, with the dotted and dashed lines respectively indicating the calculated admittance for upper (5.8 km) and lower (3.8 km) bounds on T_e, outside which $H > 2H_{\min}$. These limits are shown in (d) by dotted and dashed lines. $T_e = 4.8^{\uparrow 5.8}_{\downarrow 3.8}$ km; $H_{\min} = 0.54$ ($\rho_u = 2860$ kg m^{-3}; $F_2 = 0.15$).

function of T_e between observed and modelled gravity and topography are broad, and are consistent with lower elastic thicknesses. Using a continuous elastic plate of thickness 0–50 km to model five Bouguer anomaly profiles across the Baikal rift, Petit *et al.* (1997) also show that minima in the gravity misfit as a function of T_e are shallow, if they exist at all, and consistent with values of T_e in the explored range.

From our estimates based on the coherent part of the free-air admittance, we conclude that the elastic thickness in the Baikal rift zone as a whole is low, and likely to lie in the range 5–20 km. Although the southwest and southeast Baikal boxes have formal values of $T_e < 10$ km and the northeast box has $T_e \sim 10$ km, we do not believe the differences between them are really resolvable. The slightly larger value in the northeast rift may be because that box contains some of the Siberian shield. McKenzie (2003) explicitly looked at the admittance over the shield itself and in eastern Siberia, and found values for T_e of $15.2^{\uparrow 19.2}_{\downarrow 11.6}$ and $20.8^{\uparrow 27.4}_{\downarrow 15.6}$ km respectively.

4 CRUSTAL THICKNESS ESTIMATES FROM INVERSION OF TELESEISMIC RECEIVER FUNCTIONS

McKenzie *et al.* (2005) suggested that the depth distribution of intraplate earthquakes within both the oceanic and continental mantle lithosphere can be explained by temperature alone, and so we would like to examine geotherms in the Baikal region. If McKenzie *et al.*

(2005) are right, the lack of moderate-sized earthquakes within the mantle lithosphere of continental shields may be attributable to the temperature structure. Beneath shields, the Moho temperature is strongly influenced by crustal heat generation and crustal thickness. Therefore to accurately estimate continental geotherms from mantle nodule data (Section 5.1), it is important to have good estimates of the Moho depth in areas from which the nodules are derived. In this section, we support our geotherm modelling in Section 5.1 using crustal thickness estimates based on the inversion of teleseismic radial receiver functions, taken from three locations on the Siberian shield (sites AIKY, CHEY and YAK, Fig. 1).

Use of receiver functions to determine crustal structure is now a well-established technique (e.g. Langston 1979; Owens *et al.* 1984; Ammon *et al.* 1990), and details of its implementation do not warrant detailed repetition here. The method we adopt is essentially the same as that used by Mitra *et al.* (2005). We used teleseismic ($\Delta = 30$–$90°$) broadband data recorded at the permanent GDSN station in Yakutsk (YAK, Fig. 1), and at two temporary Geofon stations in the middle of the Siberian shield (AIKY and CHEY, Fig. 1). True-amplitude radial receiver functions were generated using the iterative, time domain deconvolution approach of Ligorría & Ammon (1999). The results were smoothed using a Gaussian width factor of 1.0, which passes frequencies up to $\sim$0.4 Hz and results in reduced resolution of intracrustal velocity contrasts. However, the feature of most interest to us here is the Moho, which is sufficiently large and localized a velocity contrast to be revealed by this choice
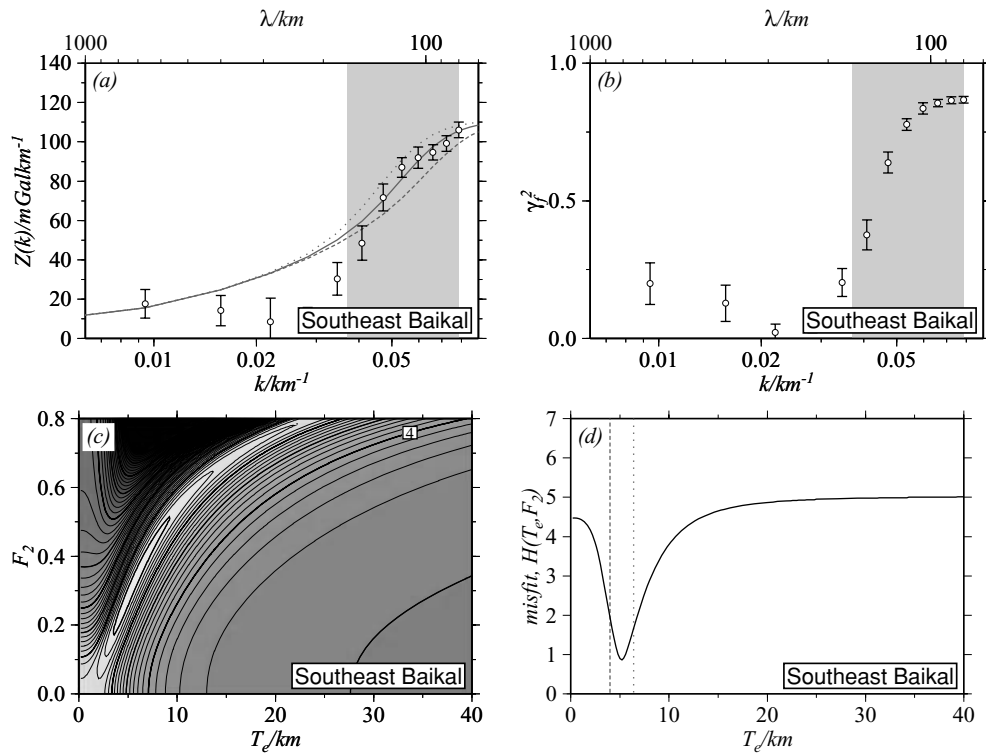
Figure 6. As for Fig. 5, but for the southeast Baikal box of Fig. 4. $80 < \lambda_{\rho_u} < 110$ km; $80 < \lambda_Z < 170$ km. Note the misfit surface in (c) defines an elongated trough, showing a trade-off between T_e and F_2; but that T_e must nonetheless be between 2 and 10 km. $T_e = 5.2^{\uparrow 6.4}_{\downarrow 4.0}$ km; $H_{\min} = 0.86$ ($\rho_u = 2660$ kg m^{-3}; $F_2 = 0.295$).
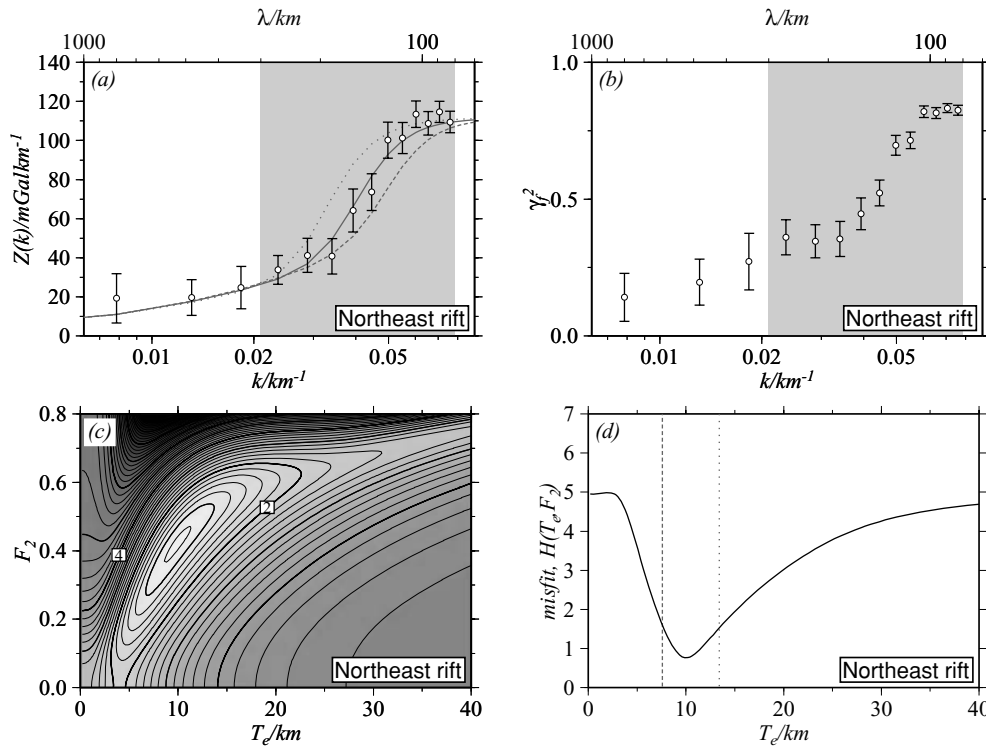

Figure 7. As for Fig. 5, but for the northeast rift box of Fig. 4. $80 < \lambda_{\rho_u} < 110$ km; $80 < \lambda_Z < 300$ km. $T_e = 10.0^{\uparrow 13.4}_{\downarrow 7.6}$ km; $H_{\min} = 0.76$ ($\rho_u = 2660$ kg m^{-3}; $F_2 = 0.425$).
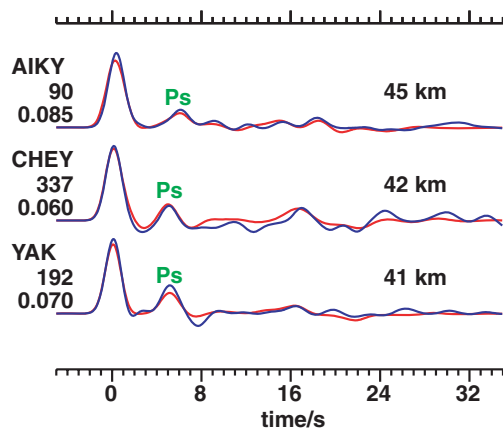
Figure 8. Selected stacked radial receiver functions for each of the three sites we have studied (AIKY, CHEY, YAK; Fig. 1). We show the observed receiver function in blue and the synthetic, produced using our final velocity model, in red. Beneath each station name we give the mean back azimuth and mean ray parameter (in s km^{-1}) for all events used in the stack. The receiver function for CHEY is from a single event. The peak we interpret as the *Ps* conversion from the Moho is clearly visible in each receiver function and is labelled in green. Alongside each receiver function, we present the determined Moho depth, all of which are uncertain by approximately ±5 km. Further details are given in the Appendix, Section C.

of filter at all three of the sites we have studied. Radial receiver functions from similar epicentral distances and back azimuths were stacked prior to inversion wherever possible.

Using the algorithm of Herrmann (2003), we determined details of the crustal structure by inverting the averaged radial receiver functions. For all three stations we discuss below, the *S*-wave velocity (V_s) is the free parameter in the inversion, with the *P*-wave velocity (V_p) given by the V_p/V_s ratio, which we fix at 1.73. Our starting models were all half-spaces of uniform *S*-wave velocity. We tested initial values of V_s between 3.12 and 4.73 km s^{-1}, the latter being a typical upper mantle velocity, and the former a slow crustal one. Receiver functions and synthetics at each station are shown in Fig. 8, which is designed to show the clear identification of the *Ps* conversion from the Moho, the principal object of interest here. Details of the data stacks and inversions at each station are given in the Appendix (Section C).

The temporary Geofon station AIKY is ~80 km from a kimberlite pipe in the Siberian shield at Udachnaya (label U, Fig. 1). Given the proximity of these two sites, receiver functions at AIKY are likely to provide an accurate constraint on the crustal thickness at Udachnaya. Using a uniform initial *S*-wave velocity of 3.82 km s^{-1}, an inversion of two receiver function stacks indicates that the crust beneath AIKY is 46–52 km thick (Fig. A19). Starting models with $V_s = 3.12$ and 4.73 km s^{-1} yield Moho depths in the 40–46 and 48–54 km ranges respectively, showing the trade-off between velocity and depth that is well known in receiver function inversions (Ammon *et al.* 1990), and the likely range of Moho depths. All inversions suggest the mid-crust to be almost uniform, with a low-velocity layer in the upper 6–10 km. Given the lack of suitable data and relatively poor signal-to-noise ratio in the stacks we have used, we are unable to reliably constrain this apparent feature any further. We estimate the crustal thickness at AIKY to be between 40 and 50 km.

Only a few high-quality receiver functions were available for the temporary Geofon station CHEY (Fig. 1), produced from events that were sparsely distributed in back azimuth and epicentral distance. Consequently, it was not possible to stack receiver functions for rays

that sample similar structure between event and receiver. Instead, we used the three best-quality individual receiver functions in a joint inversion. Starting with a uniform V_s of 3.82 km s^{-1}, we estimated the Moho to lie between 40 and 44 km depth (Fig. A20), though varying the initial *S*-wave velocities between 3.12 and 4.73 km s^{-1} show the base of the crust to lie between 38–42 and 41–46 km respectively. Therefore, the crustal thickness is likely to lie in the 38–46 km range. As with station AIKY, the receiver functions reveal the crust at CHEY to be approximately uniform, with the possible exception of a low-velocity layer in the top few kilometres.

Data are far more abundant for the permanent GDSN station YAK (Fig. 1), and we were able to stack receiver functions from teleseismic events spanning a wide range of epicentral distances and back azimuths (inset map, Fig. A21). Although it lies ~500 km from the region of interest here, a study of the velocity structure at YAK gives us some idea about how uniform the crust is likely to be across the Siberian shield. The inversion presented in Fig. A21 again uses an initial *S*-wave velocity of 3.82 km s^{-1}, and yields a Moho depth in the range 36–44 km. Initial V_s values between 3.12 and 4.73 km s^{-1} show the Moho to be at 36–42 and 37–46 km respectively. We conclude that the crustal thickness at YAK is in the range 36–46 km. A small peak observed prior to the *Ps* conversion in several receiver function stacks suggests that there may be a mid-crustal velocity discontinuity at this site.

Our results, combined with the receiver function analysis of Gao *et al.* (2004, profiles NS and WE, Fig. 1) and deep seismic sounding studies by Suvorov *et al.* (2002), allow us to estimate crustal thicknesses on the Siberian shield to an accuracy sufficient for the purposes of thermobarometric modelling (Section 5.1). We estimate that the shield has a crustal thickness in the range 40–45 km. Sparse data at two sites (AIKY, CHEY) in the middle of the shield suggest that the crust there lacks any major intracrustal velocity contrast, although there is some evidence for a mid-crustal discontinuity at station YAK further to the east. These simple analyses support the crustal thicknesses we have chosen to model the geotherm at two sites on the Siberian shield.

5 LITHOSPHERE STRUCTURE

5.1 Steady state geotherms fitted to geochemical nodule data

McKenzie *et al.* (2005) suggest that the mechanical behaviour of oceanic and continental mantle appears to depend on temperature alone, and that there is, as yet, no convincing evidence that any compositional contrasts have significant rheological effects. In order to assess this conclusion for the Lake Baikal region, we have modelled four geotherms at locations both within and outside the Siberian shield (sites U, O, V, and T, Figs 1 and 10). We used the technique of McKenzie *et al.* (2005) to fit steady state geotherms to pressure and temperature estimates from geochemical nodule data. This technique differs from previous studies of the continental geotherm (e.g. Artemieva & Mooney 2001) in that the thermal conductivity of the mantle is allowed to change with temperature, and varies by a factor of ~2 over the temperature range of interest (Schatz & Simmons 1972; Hofmeister 1999; Xu *et al.* 2004). In addition, the potential temperature of the mantle is fixed everywhere at 1315°C, which produces an oceanic crust 7 km thick by decompression melting, based on the expressions of McKenzie & Bickle (1988) using an entropy of melting of 400 JK^{-1} (Kojitani & Akaogi 1997). Furthermore, the radiogenic heat production is not
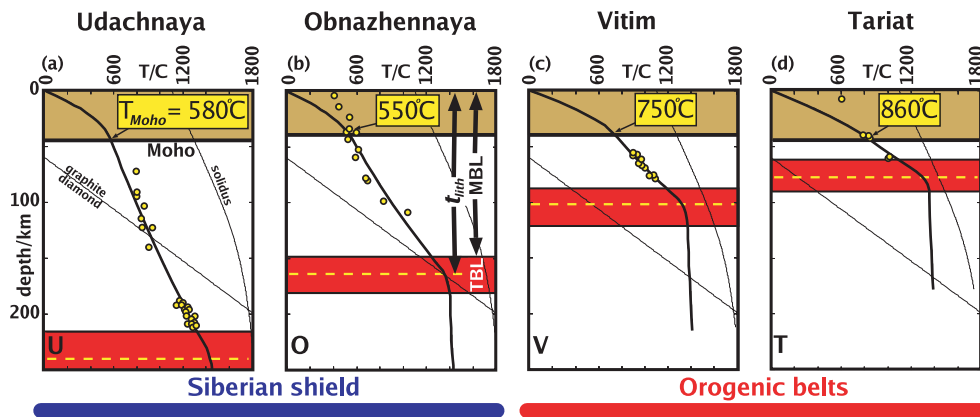
Figure 9. Geotherms fitted to pressure and temperature estimates from nodules. The technique used to fit the thermobarometric data is described in detail by McKenzie *et al.* (2005). Pressure (depth) and temperature estimates are obtained from nodule compositions using the expressions of Finnerty & Boyd (1987). Nodule locations for Udachnaya (a), Obnazhennaya (b), Vitim (c) and Tariat (d) are labelled in Figs 1 and 10 as U, O, V and T respectively. The original nodule data are from Boyd *et al.* (1997 U, intruded during the late Devonian/early Carboniferous), Taylor *et al.* (2003 O, late Jurassic), Ionov *et al.* (1993 V, Cenozoic) and Kopylova *et al.* (1995 T, Cenozoic). We use a crustal thickness of 40 km for O and V, and 45 km for U and T, in agreement with values from receiver functions, where available (Section 4 and Fig. 1). The crust is coloured in light brown, and estimated Moho temperatures (T_{Moho}) are labelled for each site. The red band shows the thermal boundary layer (TBL) used to match up advective heat transport in the convecting interior with conductive transport in the overlying mechanical boundary layer (MBL). [At Udachnaya, the base of the TBL (not shown) is 255 km deep.] We take the thickness of the thermal lithosphere (t_{lith}) to be the depth at which the conductive and convective geotherms would meet in the absence of a thermal boundary layer, shown by a dashed yellow line within each of the thermal boundary layers. The sites Udachnaya and Obnazhennaya are situated on the shield and have a considerably colder temperature structure at depths <150 km than those from the more active orogenic belts, which also have a markedly slower *S*-wave velocity at these depths (Fig. 10).

concentrated at upper crustal depths, in agreement with detailed studies of heat flow and radioactivity on the Canadian shield (Jaupart *et al.* 1998; Jaupart & Mareschal 1999; Mareschal & Jaupart 2004). Deeper radiogenic heat production within the crust means that the crustal thickness has a more pronounced effect on the Moho temperature. We therefore used receiver function estimates of crustal thickness (Section 4) wherever possible. Conductive heat transport in the lithosphere is matched up with convective transport in the underlying isentropic asthenosphere using a thermal boundary layer (labelled TBL in Fig. 9), which allows the temperature and heat flux to be continuous at all depths. The value of 'lithosphere thickness' (t_{lith}) labelled in Fig. 9 corresponds to the depth at which the conductive geotherm would meet the convective one in the absence of a thermal boundary layer.

As the geotherms presented in Fig. 9 show, there is a marked difference between the lithospere beneath the ancient continental shields (sites U and O) and the younger orogenic belts (V and T). At depths shallower than ~150 km, the sites on the shields have a considerably colder structure than those on the Palaeozoic fold belts. The lithosphere beneath the Siberian shield (U,O) is also much thicker. Within the shield (U,O), the Moho temperature is ≳550°C; outside the shield it is higher (~750°C at Vitim, ~850°C at Tariat). Given the temperature structures we have estimated, it is no surprise that the seismicity beneath Mongolia is predominantly shallow (Bayasgalan *et al.* 2005), as crustal and mantle temperatures at Tariat are predicted to be high. Furthermore, the deeper seismicity that we observe in the northeast Baikal rift is consistent with a cooler temperature structure, intermediate between those at Udachnaya and Obnazhennaya (U, O) and those at Vitim and Tariat (V, T), which may be related to its situation adjacent to the much colder Siberian shield.

Previous thermobarometric studies of the Vitim and Tariat volcanic fields agree well with the estimates of lithosphere thermal structure presented in this section. Analyses of xenoliths from both Vitim (Poort *et al.* 1998; Ionov 2002) and Tariat (Ionov 2002) produce geotherms corresponding to lithospheric thicknesses that lie

within ~10 per cent of our estimated values. Ionov (2002) estimated that the difference in temperature between sites on the Siberian shield and the fold belts to the south is ~400°–550°C at depths of 45–80 km. The corresponding difference from our own estimates of the temperature variation with depth is ~500°–600°C. Predicted Moho temperatures are also very similar: Ionov (2002, Vitim and Tariat) and Poort *et al.* (1998, Vitim) both estimate temperatures to be ~800°–900°C at depths corresponding to the base of the crust; we estimate them to be ~750°–850°C. Ionov (2002) also uses the composition of garnet-bearing peridotites from Pleistocene basalts in northern Hentei (adjacent to the eastern end of profile WE in Fig. 1) and eastern Sayan to suggest that the thermal state of the lithosphere is similar at these sites to that at Tariat in the corresponding depth range. This suggests that the temperature profiles V and T presented in Fig. 9 are characteristic of a wider region of the fold belts than simply the locations from which they were derived.

The lithospheric thickness of ~350 km found by Artemieva & Mooney (2001) for the oldest parts of the Siberian shield differs significantly from our estimated value of ~240 km from Udachnaya (U, Figs 1, 9 and 10), whereas their estimate of ~150–200 km at the northeastern boundary of the craton agrees with our estimate of ~170 km at Obnazhennaya (O, Figs 1, 9 and 10). Our estimates of lithospheric thickness are supported by results from the tomographic wave speed model of Priestley *et al.* (2006; see Section 5.2 and Fig. 10 in this study), which uses fundamental and higher mode regional waveforms. One possible source of the discrepancy between our results and those of Artemieva & Mooney is the contribution of crustal radiogenic heat production to the observed surface heat flow. Mareschal & Jaupart (2004) show that variations in crustal heat production can account for large changes in observed heat flow with no significant change in lithospheric thickness. It is plausible, therefore, that the larger thermal thicknesses of the lithosphere estimated by Artemieva & Mooney are due, at least in part, to reduced crustal heat production and its effect on the surface heat flow.
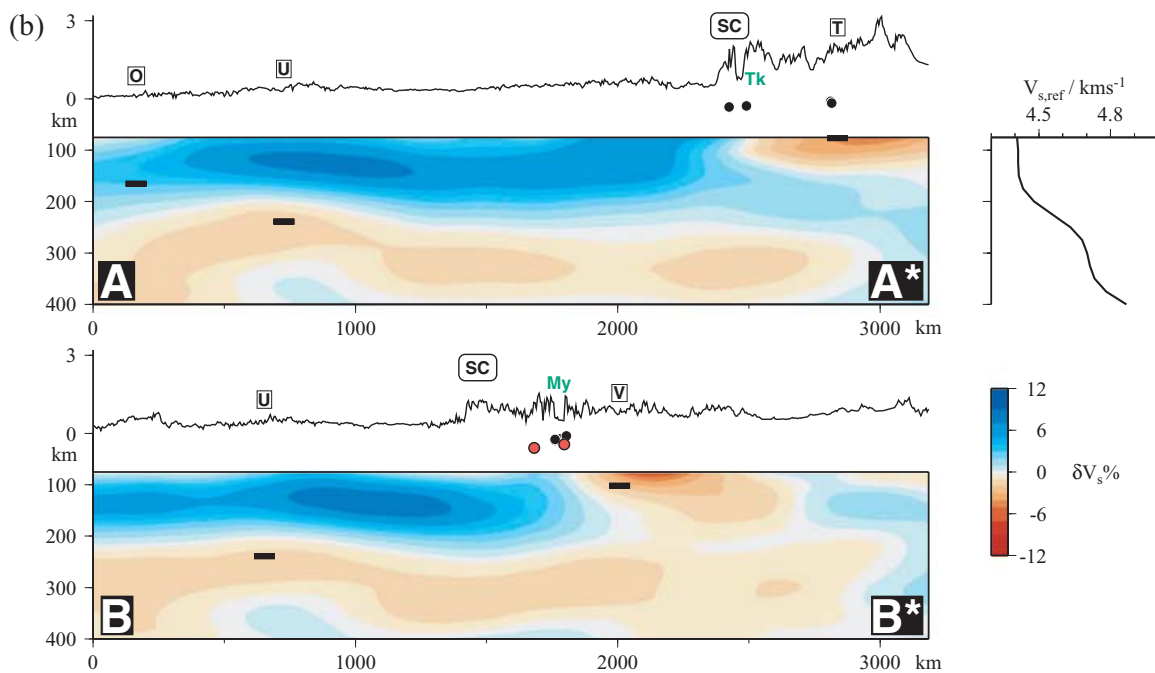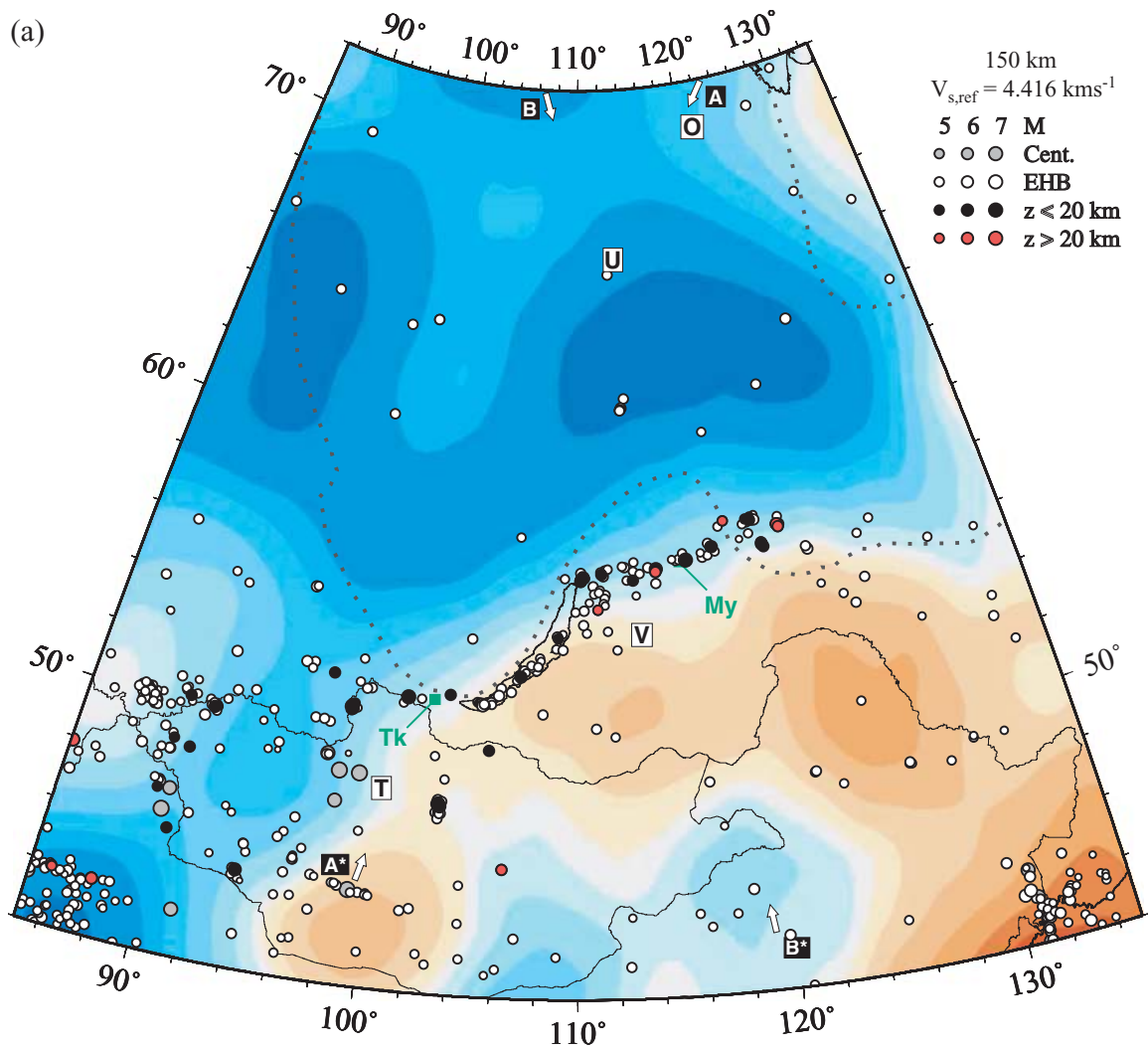
5.2 Surface wave tomography

Velocity structure obtained from surface waves is often a good indicator of contrasts in lithosphere properties on the continents (e.g. Ritzwoller & Levshin 1998; Ritsema & van Heijst 2000). Ancient, cold, inactive cratonic lithosphere generally has a faster velocity structure than the actively deforming mountain belts. Where multimode surface waves are used to measure such contrasts in tomographic inversions, the depth resolution of the models is greatly improved, as these waves are more sensitive to the upper few hundred kilometres of the Earth's mantle (Debayle *et al.* 2001; Gung *et al.* 2003; Priestley & Debayle 2003; Debayle *et al.* 2005).

Here, we present the *Sv* wave speed tomographic model of Priestley & Debayle (2003) and Priestley *et al.* (2006), which uses regional waveforms of the fundamental and first four higher modes to image the upper mantle at depths up to ~400 km. A slice through the velocity model at a depth of 150 km clearly shows the contrast between the upper mantle beneath the active orogenic belts and that of the cold, fast Siberian shield (Fig. 10). Although the data are smoothed on a horizontal lengthscale of ~400 km, there is a clear correlation between the locations of earthquake epicentres and the velocity contrast that marks the Siberian shield boundary. This is also the trend followed by the right-stepping *en echelon* basins of the northeast rift zone (e.g. Logatchev 1993). It appears from Fig. 10 that the geologically mapped boundary of the Siberian shield at the surface (dotted line) may provide a poor description of the shield edge at depth, though the lateral resolution (~400 km) of the velocity model should be kept in mind. Profiles AA* and BB* in Fig. 10 are vertical sections through the tomography model, coloured only below 75 km, with topography added in vertical exaggeration. These profiles show further how seismicity is concentrated at the edge of the shield, as defined by the tomography. Of particular interest is section BB*, where the geologically located shield edge at the surface (which correlates with topography) does not coincide with our interpretation of that edge at depth. A simple interpretation of this difference is that younger rocks to the south have been thrust onto the shield in the north, obscuring its boundary beneath the surface. This is supported by the presence of an arcuate series of post-accretionary thrusts observed as far north as 60°N (e.g. Bulgatov & Gordienko 1999; Parfenov *et al.* 1995, 2004), and by a negative free-air gravity anomaly to the northwest of the Vitim embayment (around line PQ in Fig. 4c). Although this depression in the gravity field lacks the asymmetry of a flexed foreland (it is roughly symmetric about line PQ), it is possible that some of the signal has been removed by erosion and infill. It is also possible that the course taken by the northeasterly flowing Lena river has been affected by the downward flexure of the shield that this loading has caused, as it now

parallels the range front of the Vitim embayment between ~109°–119°E (Fig. 1). An analogous situation to this proposed overthrusting probably exists in the Himalayas, where the Indian shield is thrust ~300 km north of its surface limit beneath southern Tibet (Sandvol *et al.* 1997; Chen & Özalaybey 1998; Huang *et al.* 2000; DeCelles *et al.* 2002; Jackson *et al.* 2004).

Profiles AA* and BB* (Fig. 10) pass close to the four sites from which geochemical nodules and geotherm estimates were derived. Superposed on the *S*-wave velocity structure we show estimates of the lithosphere thickness (t_{lith}) obtained from the geotherm modelling. The defined base of the lithosphere revealed by the tomography is expected to lie in the thermal boundary layer (TBL, Fig. 9) beneath the colder, faster lithosphere. There is a good agreement between the general features of the lithosphere estimated using the two techniques. For example, the lithosphere beneath Udachnaya (site U, Fig. 10) is predicted by the geotherm modelling to be cold and ~240 km thick, and this is reflected in a fast velocity anomaly extending to ~200 km depth. Both the thermal structure and the velocity structure suggest that the Baikal rift zone is a region across which an abrupt change in lithosphere thickness occurs.

6 DISCUSSION

In our study of the seismogenic thickness (T_s) along the Baikal rift zone we have shown that the whole crust is seismogenic, and that there is no strong evidence showing the mantle to be a significant source of seismicity. T_s along the rift zone itself is larger than that of Mongolia to the southwest, where, with the exception of one event (980924, Table 1), there is no evidence for earthquake centroid depths greater than 20 km (Bayasgalan *et al.* 2005).

Apart from a single event having complicated waveforms (990225, M_w 5.9, Table 2), which most probably nucleated within the crust (see the caption to Table 2 and the Appendix, Section B), and one event (051211, M_w 5.7, Table 2) whose seismograms—though consistent with a relatively shallow focus (see the Appendix, Section B)—were contaminated by high levels of noise, we have been able to model all events with $M_w > 5.5$, as well as several smaller ones. None of our modelled events has a centroid depth exceeding 30 km. Indeed, although microearthquakes relocated by local networks have depths up to ~40 km and greater, the vast majority of such events are located in the upper 30 km of the crust (Radziminovich *et al.* 2003). It is possible that the lower 10 km of the crust is too hot for earthquakes with $M_w > 5.5$ to occur there, and that seismicity is restricted to relatively few earthquakes of smaller magnitude as a result.

2-D admittance analysis of gravity and topography data yields low values of ~10 km or less for the effective elastic thickness (T_e)

Figure 10. (a) The fundamental and higher-mode *Sv* wave speed tomographic model of Priestley & Debayle (2003) and Priestley *et al.* (2006). Percentage velocity deviations (see scale, bottom right panel b) are shown at a depth of 150 km, relative to a reference velocity of 4.416 km s^{-1}. Earthquakes with good depth control (from Bayasgalan *et al.* 2005, and this study) are shown as red or black circles, coloured according to depth using the same scheme as Fig. 2 (see legend). Other epicentres are shown as white or grey circles. The geologically mapped boundary to the Siberian shield is marked with a dotted line, as in Fig. 1. (b) Profiles AA* and BB*, showing velocity perturbations relative to a smoothed version of the preliminary reference earth model (PREM, Dziewonski & Anderson 1981), displayed to the right of profile AA*. Thick black bars beneath nodule sites O, U, T and V show estimates of the lithosphere thickness (t_{lith}), determined from the geotherms we have modelled (Section 5.1). The approximate position of the shield boundary mapped at the surface is marked SC and correlates with an abrupt change in elevation. In profile BB*, the geologically mapped edge to the shield at the surface is clearly different from the tomographic signature of the same feature at depth. Earthquakes whose depths have been determined by waveform modelling are shown if their epicentres lie within ±200 km of a profile, and are coloured red if they are more than 20 km deep. In both profiles, the rift-related earthquakes are concentrated at the shield edge, as defined by the tomography. The rift basins (Tunka, **Tk**, profile AA*; Muya, **My**, profile BB*) are situated above the same feature. The abrupt change in elevation seen close to the geologically mapped shield boundary at the surface, as well as the discrepancy between this boundary and its tomographic signature at depth, can be explained by thrusting of younger rocks on top of the ancient Siberian shield, which would obscure its boundary at the surface.

in three regions surrounding the rift zone. Based on T_e estimates for the eastern Siberia, the Siberian shield (McKenzie 2003), and those from this study, we infer that the elastic thickness of the seismically active part of the rift system is also low, with a value <20 km. T_e is thus comparable to T_s. Our values of T_e are lower than those determined with the Bouguer coherence technique of Forsyth (1985), used by Diament & Kogan (1990) and Ruppel *et al.* (1993), who find values of ~30 and 40–60 km respectively. However, it has been argued (McKenzie 2003) that these estimates provide only an upper bound on the elastic thickness. Nowhere does our analysis require that $T_e > T_s$, and so our results are in agreement with the pattern of T_e and T_s values reported by Maggi *et al.* (2000a). There is no evidence implying that the mantle of the Baikal rift zone is a significant source of elastic strength, either on the timescale of the earthquake cycle or over the periods for which topographic loads are supported elastically.

Earthquakes along the rift zone form an approximately linear band of concentrated seismicity up to ~200 km wide in places, trending SW–NE from southwest Lake Baikal out to ~123°E (Fig. 1). The topographic expression of the rift basins also follows this trend (Figs 1 and 2). It is difficult to explain the localization of these seismotectonic features if the Proterozoic–Palaeozoic suture at the edge of the Siberian shield lies along the dotted line shown in Figs 1, 2 and 10. Although the line we present shows only an approximate geologically mapped position, similar shapes are presented throughout the literature (e.g. Logatchev & Florensov 1978; Goodwin 1991; Logatchev 1993). Publications regularly show the characteristic S-shaped shield boundary paralleling Lake Baikal before turning north for ~300 km, following the abrupt change in topographic relief around the Vitim embayment (Fig. 1) instead of the *en echelon* rift basins in the northeast rift zone (fig. 5 of Petit *et al.* 1996, shows this especially clearly). We now suspect that a feature of this shape provides a poor description of the shield edge at depth. The earthquake epicentres in the northeast rift seemingly delineate the shield boundary at depth as far east as ~123°E. In Fig. 10 there is a distinct contrast between the fast velocities of the cold Siberian shield and the relatively slow velocities beneath Mongolia and the Sayan-Baikal foldbelt. The correlation between the rift-related epicentres and the edge of the Siberian shield, as shown by the velocity structure, is also clear. It seems that the stable lithospheric root of the shield plays a greater rôle in the location of the rift zone than geological estimates of the shield boundary would otherwise suggest. This revised position for the edge of the shield may explain why we measure a slightly larger elastic thickness in the northeast rift zone, as about half of the northeast box (Figs 1 and 4c) is underlain by the Siberian shield at depth, as defined by the tomographic boundary. In the event that the velocity structure *does* show the subsurface edge of the Siberian shield, there is no need to explain the northeasterly termination of the rift structures in terms of the rift entering the thicker lithosphere and 'incompatible' structural grain of the Archean Aldan shield in the northeast, as suggested by Logatchev & Florensov (1978). Instead, the northeasterly decay of rifting and seismicity could be explained by the fact that distance to the pole of relative rotation between Siberia and Amuria decreases with increasing distance northeast of the rift zone (see England & Molnar 2005).

The discrepancy between the tomographic and geological estimates of the shield boundary can be explained by past tectonic episodes, thrusting material onto the shield's surface. The presence of an arcuate series of post-accretionary thrust faults within the Vitim embayment supports this hypothesis, as does the negative free-air gravity anomaly paralleling the embayment range front (line PQ in Fig. 4c), which may be the eroded and infilled remainder of a flexed foreland basin. If overthrusting concealment processes, such as those we believe to have occurred here, are common in other global settings, it is conceivable that the boundaries of Precambrian shields have a greater effect on the location of seismically deforming zones than is apparent from the surface geology.

McKenzie *et al.* (2005) suggest that temperature is probably the sole factor controlling whether the mantle is seismogenic beneath both the oceans and continents. They conclude that intraplate earthquakes with $M_w > 5.5$ are unlikely to occur at temperatures >600°C, unless strain rates are high. Beneath the Siberian shield, at Udachnaya and Obnazhennaya (U and O, Fig. 1), we estimate Moho temperatures to be ≳550°C, so the lack of moderate mantle earthquakes there is not surprising. At Vitim (V, ~750°C) and Tariat (T, ~850°C), the Moho temperature is higher, and it has been suggested that the lithosphere has a similar thermal state at other fold belt sites surrounding the southern edge of the Siberian shield (Ionov 2002). Recent work by Priestley & McKenzie (2006) indicates that there is a well-defined relationship between *S*-wave velocity and temperature at upper mantle depths. The *S*-wave velocities shown in Fig. 10 suggest an intermediate temperature structure in the seismically active part of the rift system, between that of the Siberian shield (positions U and O; geotherms 9a and 9b) and the foldbelt to the south (position V and T; geotherms 9c and 9d), though the rift itself is too small to show up in the tomography. Using Priestley and McKenzie's expressions, we estimate the temperature at a depth of 100 km beneath the rift system to be 1000°–1300°C, making it slightly cooler than the geotherm at Vitim (Fig. 9c), but still with a Moho temperature greater that 600°C. Given that the mantle temperature beneath the seismically active part of the rift is likely to exceed that beneath the Siberian shield to the north, and given that the mantle beneath the Siberian shield is apparently too hot to be seismogenic, it seems that temperature structure alone can indeed account for the apparent scarcity of mantle seismicity beneath the Baikal rift zone. The deeper seismicity that we observe in the northeast Baikal rift is consistent with a cooler crustal temperature structure, which may be related to its situation adjacent to the much colder Siberian shield. One anomalous lower-crustal earthquake, separated from the main lower-crustal activity in the northeast rift, is a M_w 5.5 event at a depth of 27 km (980924, Table 1), located within a structure delineated by a ~50 × 150 km band of concentrated microseismicity in central Mongolia. This anomalous feature is too small to be detected by the tomography study of Fig. 10. We conclude that, given the relatively high temperatures beneath Mongolia and the Baikal rift zone, it is no surprise that the mantle there is comparatively, if not almost entirely, aseismic and not a source of long-term elastic strength.

7 CONCLUSIONS

This study demonstrates that it is possible to combine diverse data from several different sources, such as seismicity, gravity, topography and thermal and velocity structures, into a coherent, simple, picture of continental lithosphere rheology. Earthquakes within the Baikal rift system are restricted to the crust, with the possible exception of a few low-magnitude events occurring beneath the Moho. Larger, lower-crustal earthquakes appear to be concentrated in the northeast. The mantle in the Baikal region is not a significant source of seismicity and all events with $M_w > 5.5$ have been found to occur in the crust, as expected from geotherm estimates of Moho temperatures, which everywhere exceed 600°C beneath the

seismically active part of the rift. Free-air admittance estimates of effective elastic thickness within, and in all regions adjacent to, the Siberian shield are all less than 30 km, with values less than 20 km found either side of the rift zone. The elastic thickness is therefore comparable to, or less than, the seismogenic thickness everywhere in the Baikal region. From these observations there is no reason to believe that the mantle in this area is a source of long-term strength in the lithosphere.

In Mongolia, Siberia and Transbaikalia there is a remarkable consistency between the lithosphere velocity structure determined by multimode surface wave tomography, the geotherms estimated from mantle nodules, and the localization of seismicity. This, in turn, indicates that the geological and topographic position of the Siberian shield edge at the surface may not represent that boundary at depth. This discrepancy may be the result of earlier overthrusting of younger rocks onto the ancient shield, analogous to the situation in the Himalayas and southern Tibet.

ACKNOWLEDGMENTS

REFERENCES

Ammon, C., Randall, G. & Zandt, G., 1990. On the nonuniqueness of receiver function inversions, *J. geophys. Res.,* **95**(10), 15 303–15 318.

Artemieva, I. & Mooney, W., 2001. Thermal thickness and evolution of Precambrian lithosphere: a global study, *J. geophys. Res.,* **106**(8), 16 387–16 414, doi:10.1029/2000JB900439.

Bayasgalan, A. & Jackson, J., 1999. A re-assessment of the faulting in the 1967 Mogod earthquakes in Mongolia, *Geophys. J. Int.,* **138**(3), 784–800.

Bayasgalan, A., Jackson, J. & McKenzie, D., 2005. Lithosphere rheology and active tectonics in Mongolia: relations between earthquake source parameters, gravity and GPS measurements, *Geophys. J. Int.,* **163**(3), 1151, doi:10.1111/j.1365-246X.2005.02764.x.

Boyd, F., Pokhilenko, M., Pearson, D., Mertzman, S., Sobolev, N. & Finger, L., 1997. Composition of the Siberian cratonic mantle: evidence from Udachnaya peridotite xenoliths, *Contrib. Mineral. Petrol.,* **128**(2–3), 228–246, doi:10.1007/s004100050305.

Brace, W. & Kohlstedt, D., 1980. Limits on lithospheric stress imposed by laboratory experiments, *J. geophys. Res.,* **85**(11), 6248–6252.

Brazier, R. & Nyblade, A., 2003. Upper mantle P velocity structure beneath the Baikal Rift from modeling regional seismic data, *Geophys. Res. Lett.,* **30**(4), 1153, doi:10.1029/2002GL016115.

Bulgatov, A. & Gordienko, I., 1999. Preliminary terrane and overlap assemblage map of Transbaikalia and eastern Sayan region, southern Siberia, Russia, *USGS open-file report OF 99-165,* 1 sheet.

Burov, E. & Diament, M., 1995. The effective elastic thickness (T_e) of continental lithosphere: what does it really mean?, *J. geophys. Res.,* **100**(3), 3905–3927.

Burov, E., Houdry, F., Diament, M. & Déverchère, J., 1994. A broken plate beneath the north Baikal rift revealed by gravity modelling, *Geophys. Res. Lett.,* **21**(2), 129–132.

Chapman, C., 1978. A new method for computing synthetic seismograms, *Geophys. J. R. astr. Soc.,* **54,** 481–518.

Chapman, C., Yen-Yi, C. & Lyness, D., 1988. The WKBJ seismogram algorithm, in *Seismological algorithms: Computational methods and computer programs,* chap. I.2, pp. 47–74, ed. Doornbos, D., Academic Press Limited, London.

Chen, W.-P. & Molnar, P., 1983. Focal depths of intracontinental and intraplate earthquakes and their implications for the thermal and mechanical properties of the lithosphere, *J. geophys. Res.,* **88,** 4183–4214.

Chen, W.-P. & Özalaybey, S., 1998. Correlation between seismic anisotropy and Bouguer gravity anomalies in Tibet and its implications for lithospheric structures, *Geophys. J. Int.,* **135**(1), 93–101.

Crosby, A., 2006. Aspects of the relationship between topography and gravity on the Earth and Moon, *PhD thesis,* University of Cambridge.

Debayle, E., Lévêque, J. & Cara, M., 2001. Seismic evidence for a deeply rooted low-velocity anomaly in the upper mantle beneath the northeastern Afro/Arabian continent, *Earth planet. Sci. Lett.,* **193**(3–4), 423–436.

Debayle, E., Kennett, B. & Priestley, K., 2005. Global azimuthal seismic anisotropy and the unique plate-motion deformation of Australia, *Nature,* **433,** 509–512, doi:10.1038/nature03247.

DeCelles, P., Robinson, D. & Zandt, G., 2002. Implications of shortening in the Himalayan fold-thrust belt for uplift of the Tibetan Plateau, *Tectonics,* **21**(6), 1062, doi:10.1029/2001TC001322.

Delouis, B., Déverchère, J., Melnikova, V., Radziminovitch, N., Loncke, L., Larroque, C., Ritz, J. & San'kov, V., 2002. A reappraisal of the 1950 (M_w 6.9) Mondy earthquake, Siberia, and its relationship to the strain pattern at the south-western end of the Baikal rift zone, *TerraNova,* **14**(6), 491–500.

Déverchère, J., Houdry, F., Diament, M., Solonenko, N. & Solonenko, A., 1991. Evidence for a seismogenic upper mantle and lower crust in the Baikal rift, *Geophys. Res. Lett.,* **18,** 1099–1102.

Déverchère, J., Houdry, F., Solonenko, N., Solonenko, A. & Sankov, V., 1993. Seismicity, active faults and stress field of the North Muya Region, Baikal rift: new insights on the rheology of extended continental lithosphere, *J. geophys. Res.,* **98**(11), 19 895–19 912.

Déverchère, J., Petit, C., Gileva, G., Radziminovitch, N., Melnikova, V. & San'kov, V., 2001. Depth distribution of earthquakes in the Baikal rift system and its implications for the rheology of the lithosphere, *Geophys. J. Int.,* **146,** 714–730.

Diament, M. & Kogan, M., 1990. Long wavelength gravity anomalies and the deep thermal structure of the Baikal rift, *Geophys. Res. Lett.,* **17**(11), 1977–1980.

Doser, D., 1991a. Faulting within the western Baikal rift as characterized by earthquake studies, *Tectonophysics,* **196,** 87–107.

Doser, D., 1991b. Faulting within the eastern Baikal rift as characterized by earthquake studies, *Tectonophysics,* **196,** 109–139.

Doser, D. & Yarwood, D., 1994. Deep crustal earthquakes associated with continental rifts, *Tectonophysics,* **229,** 123–131.

Dziewonski, A. & Anderson, D., 1981. Preliminary reference Earth model, *Phys. Earth planet. Inter.,* **25,** 297–356, doi:10.1016/0031-9201(81)90046-7.

Dziewonski, A., Chou, T. & Woodhouse, J., 1981. Determination of earthquake source parameters from waveform data for studies of global and regional seismicity, *J. geophys. Res.,* **86,** 2825–2852.

Ebinger, C. & Hayward, N., 1996. Soft plates and hot spots: Views from Afar, *J. geophys. Res.,* **101**(10), 21 859–21 876.

Ekström, G., 1994. Rapid earthquake analysis utilizes the internet, *Computers in Physics,* **8,** 632–638.

Ekström, G. & England, P., 1989. Seismic strain rates in regions of distributed continental deformation, *J. geophys. Res.,* **94**(8), 10 231–10 257.

Engdahl, E. & Villaseñor, A., 2002. Global seismicity: 1900-1999, in *International Handbook of Earthquake and Engineering Seismology, Part A,* chap. 41, pp. 665–690, eds Lee, W., Kanamori, H., Jennings, P. & Kisslinger, C., Academic Press Limited, London.

Engdahl, E., Van der Hilst, R. & Buland, R., 1998. Global teleseismic earthquake relocation with improved travel times and procedures for depth determination, *Bull. seism. Soc. Am.,* **88**(3), 722–743.

England, P. & Molnar, P., 2005. Late Quaternary to decadal velocity fields in Asia, *J. geophys. Res.,* **110,** B12401, doi:10.1029/2004JB003541.

Finnerty, A. & Boyd, F., 1987. Thermobarometry for garnet peridotites and compositional structure of the upper mantle, in *Mantle Xenoliths,* pp. 381–402, J. Wiley & Sons, New York.

Forsyth, D., 1985. Subsurface loading and estimates of the flexural rigidity of continental lithosphere, *J. geophys. Res.,* **90**(14), 12 623–12 632.

Gao, S. *et al.*, 1994a. Asymmetric upwarp of the asthenosphere beneath the Baikal rift zone, Siberia, *J. geophys. Res.,* **99**(8), 15 319–15 330.

Gao, S., Davis, P., Liu, H., Slack, P., Zorin, Y., Mordvinova, V., Kozhevnikov, V. & Meyer, R., 1994b. Seismic anisotropy and mantle flow beneath the Baikal rift zone, *Nature,* **371,** 149–151.

Gao, S., Liu, K. & Chen, C., 2004. Significant crustal thinning beneath the Baikal rift zone: new constraints from receiver function analysis, *Geophys. Res. Lett.,* **31**(20), L20610, doi:10.1029/2004GL020813.

Goodwin, A., 1991. *Precambrian Geology: The dynamic evolution of the continental crust,* Academic Press, San Diego, California, 666 p.

Gung, Y., Panning, M. & Romanowicz, B., 2003. Global anisotropy and the thickness of continents, *Nature,* **422,** 707–711.

Herrmann, R., 2003. *Computer Programs in Seismology 3.30,* Tech. rep., Saint Louis University.

Hofmeister, A., 1999. Mantle values of thermal conductivity and the geotherm from phonon lifetimes, *Science,* **283**(5408), 1699–1706, doi:10.1126/science.283.5408.1699.

Huang, J. & Chen, W., 1986. Source mechanisms of the Mogod earthquake sequence of 1967 and the event of 1974 July 4 in Mongolia, *Geophys. J. R. astr. Soc.,* **84,** 361–379.

Huang, W. *et al.*, 2000. Seismic polarization anisotropy beneath the central Tibetan plateau, *J. geophys. Res.,* **105**(12), 27 979–27 990, doi:10.1029/2000JB900339.

Ionov, D., 2002. Mantle structure and rifting processes in the Baikal–Mongolia region: geophysical data and evidence from xenoliths in volcanic rocks, *Tectonophysics,* **351,** 41–60.

Ionov, D., Ashchepkov, I., Stosch, H.-G., Witt-Eickschen, G. & Seck, H., 1993. Garnet peridotite xenoliths from the Vitim volcanic field, Baikal region: the nature of the garnet-spinel peridotite transition zone in the continental mantle, *J. Petrol.,* **34**(6), 1141–1175.

Jackson, J., 2002. Strength of the continental lithosphere: time to abandon the jelly sandwich?, *GSA Today,* **12,** 4–10.

Jackson, J., Austrheim, H., McKenzie, D. & Priestley, K., 2004. Metastability, mechanical strength and the support of mountain belts, *Geology,* **32**(7), 625–628, doi:10.1130/G20397.1.

Jaupart, C. & Mareschal, J., 1999. The thermal structure and thickness of continental roots, *Lithos,* **48,** 93–114.

Jaupart, C., Mareschal, J., Guillou-Frottier, L. & Davaille, A., 1998. Heat flow and thickness of the lithosphere in the Canadian shield, *J. geophys. Res.,* **103**(7), 15 269–15 286, doi:10.1029/98JB01395.

Kennett, B., Engdahl, E. & Buland, R., 1995. Constraints on seismic velocities in the earth from travel times, *Geophys. J. Int.,* **122,** 108–124.

Kojitani, H. & Akaogi, M., 1997. Melting enthalpies of mantle peridotite: calorimetric determinations in the system CaO-MgO-Al$_2$O$_3$-SiO$_2$ and application to magma generation, *Earth planet. Sci. Lett.,* **153,** 209–222.

Kopylova, M., O'Reilly, S. & Genshaft, Y., 1995. Thermal state of the lithosphere beneath central Mongolia: evidence from deep-seated xenoliths from the Shavaryn-Saram volcanic centre in the Tariat depression, Hangai, Mongolia, *Lithos,* **36**(3–4), 243–255.

Langston, C., 1979. Structure under Mount Rainier, Washington, inferred from teleseismic body waves, *J. geophys. Res.,* **84**(9), 4749–4762.

Ligorría, J. & Ammon, C., 1999. Iterative deconvolution and receiver-function inversion, *Bull. seism. Soc. Am.,* **89**(5), 1395–1400.

Logatchev, N., 1993. History and geodynamics of the Lake Baikal rift in the context of the eastern Siberian rift system: a review, *Bull. Centres Rech. Explor.-Prod. Elf Aquitaine,* **17**(2), 353–370.

Logatchev, N. & Florensov, N., 1978. The Baikal system of rift valleys, *Tectonophysics,* **45**(1), 1–13.

Maggi, A., Jackson, J., McKenzie, D. & Priestley, K., 2000a. Earthquake focal depths, effective elastic thickness, and the strength of the continental lithosphere, *Geology,* **28,** 495–498.

Maggi, A., Jackson, J., Priestley, K. & Baker, C., 2000b. A re-assessment of focal depth distributions in southern Iran, the Tien Shan and northern India: do earthquakes really occur in the continental mantle?, *Geophys. J. Int.,* **143**(3), 629–661.

Mangino, S., Priestley, K. & Ebel, J., 1999. The receiver structure beneath the China digital seismograph network stations, *Bull. seism. Soc. Am.,* **89**(4), 1053–1076.

Mareschal, J. & Jaupart, C., 2004. Variations of surface heat flow and lithospheric thermal structure beneath the North American craton, *Earth planet. Sci. Lett.,* **223,** 65–77, doi:10.1016/j.epsl.2004.04.002.

McCaffrey, R. & Abers, G., 1988. SYN3: A program for inversion of teleseismic body waveforms on microcomputers, Air Force Geophysics Laboratory Technical Report AFGL-TR-0099, Hanscomb Air Force Base, Massachusetts.

McCaffrey, R. & Nábělek, J., 1987. Earthquakes, gravity, and the origin of the Bali Basin: an example of a nascent continental fold-and-thrust belt, *J. geophys. Res.,* **92**(1), 441–460.

McCaffrey, R., Zwick, P. & Abers, G., 1991. SYN4 program, *IASPEI Software Library,* **3,** 81–166.

McKenzie, D., 2003. Estimating T_e in the presence of internal loads, *J. geophys. Res.,* **108**(9), 2438, doi:10.1029/2002JB001766.

McKenzie, D. & Bickle, M., 1988. The volume and composition of melt generated by extension of the lithosphere, *J. Petrol.,* **29**(3), 625–679.

McKenzie, D. & Fairhead, D., 1997. Estimates of the effective elastic thickness of the continental lithosphere from Bouguer and free air gravity anomalies, *J. geophys. Res.,* **102**(12), 27 523–27 552.

McKenzie, D., Jackson, J. & Priestley, K., 2005. Thermal structure of oceanic and continental lithosphere, *Earth planet. Sci. Lett.,* **233**(3–4), 337–349, doi:10.1016/j.epsl.2005.02.005.

Mitra, S., Priestley, K., Bhattacharyya, A. & Gaur, V., 2005. Crustal structure and earthquake focal depths beneath northeastern India and southern Tibet, *Geophys. J. Int.,* **160**(1), 227–248, doi:10.1111/j.1365-246X.2004.02470.x.

Molnar, P. & Lyon-Caen, H., 1989. Fault plane solutions of earthquakes and active tectonics of the Tibetan Plateau and its margins, *Geophys. J. Int.,* **99,** 123–153.

Molnar, P. & Tapponnier, P., 1975. Cenozoic tectonics of Asia: Effects of a continental collision, *Science,* **189**(4201), 419–426.

Nábělek, J., 1984. Determination of earthquake source parameters from inversion of body waves, *PhD thesis,* MIT, Cambridge, Massachusetts.

Owens, T., Zandt, G. & Taylor, S., 1984. Seismic evidence for an ancient rift beneath the Cumberland plateau, Tennessee: a detailed analysis of broadband teleseismic P waveforms, *J. geophys. Res.,* **89**(9), 7783–7795.

Parfenov, L., Bulgatov, A. & Gordienko, I., 1995. Terranes and accretionary history of the Transbaikalian orogenic belts, *International Geology Review,* **37,** 736–751.

Parfenov, L. *et al.*, 2004. Generalized northeast asia geodynamics map, *USGS open-file report 2004-1252,* 1 sheet.

Pérez-Gussinyé, M., Lowry, A., Watts, A. & Velicogna, I., 2004. On the recovery of effective elastic thickness using spectral methods: Examples from synthetic data and from the Fennoscandian shield, *J. geophys. Res.,* **109**(10409), B10409, doi:10.1029/2003JB002788.

Petit, C., Déverchère, J., Houdry, F., Sankov, V., Melnikova, V. & Delvaux, D., 1996. Present-day stress field changes in the Baikal rift and tectonic implications, *Tectonics,* **15**(6), 1171–1191.

Petit, C., Burov, E. & Déverchère, J., 1997. On the structure and mechanical behaviour of the extending lithosphere in the Baikal rift from gravity modelling, *Earth planet. Sci. Lett.,* **149,** 29–42.

Petit, C., Koulakov, I. & Déverchère, J., 1998. Velocity structure around the Baikal rift zone from teleseismic and local earthquake travel times and geodynamic implications, *Tectonophysics,* **296,** 125–144.

Poort, J., van der Beek, P. & ter Voorde, M., 1998. An integrated modelling study of the central and northern Baikal rift: evidence for non-uniform lithospheric thinning?, *Tectonophysics,* **291**(1), 101–122, doi:10.1016/S0040-1951(98)00034-1.

Priestley, K. & Debayle, E., 2003. Seismic evidence for a moderately thick lithosphere beneath the Siberian Platform, *Geophys. Res. Lett.,* **30**(3), 1118, doi:10.1029/2002GL015931.

Priestley, K. & McKenzie, D., 2006. The thermal structure of the lithosphere from shear wave velocities, *Earth planet. Sci. Lett.,* **244**(1–2), 285–301, doi:10.1016/j.epsl.2006.01.008.

Priestley, K., Debayle, E., McKenzie, D. & Pilidou, S., 2006. Upper mantle structure of eastern Asia from multi-mode surface waveform tomography, *J. geophys. Res.,* in press.

Radziminovich, N., Balyshev, S. & Golubev, V., 2003. Earthquake focal depths and crustal strength in the Baikal rift, *Geologiya i Geofizika (Russian Geology and Geophysics),* **44**(11), 1214–1223.

Radziminovitch, N., Déverchère, J., Melnikova, V., San'kov, V. & Giljova, N., 2005. The 1999 M_w 6.0 earthquake sequence in the southern Baikal rift, Asia, and its seismotectonic implications, *Geophys. J. Int.,* **161**(2), 387–400, doi:10.1111/j.1365-246X.2005.02604.x.

Ritsema, J. & van Heijst, H., 2000. New seismic model of the upper mantle beneath Africa, *Geology,* **28**(1), 63–66.

Ritzwoller, M. & Levshin, A., 1998. Eurasian surface wave tomography: group velocities, *J. geophys. Res.,* **103**(3), 4839–4878, doi:10.1029/97JB02622.

Ruppel, C., Kogan, M. & McNutt, M., 1993. Implications of new gravity data for Baikal rift zone structure, *Geophys. Res. Lett.,* **20**(15), 1653–1638.

Sandvol, E., Ni, J., Kind, R. & Zhao, W., 1997. Seismic anisotropy beneath the southern Himalayas-Tibet collision zone, *J. geophys. Res.,* **102**(8), 17 813–17 824, doi:10.1029/97JB01424.

Schatz, J. & Simmons, G., 1972. Thermal conductivity of Earth materials at high temperatures, *J. geophys. Res.,* **77,** 6966–6983.

Schlupp, A., 1996. Neotectonique de la Mongolie occidentale analysée à partir de données de terrain, sismologiques et satellitaires, *PhD thesis*, Université Louis Pasteur de Strasbourg, 172 p.

Simons, F., Zuber, M. & Kerenga, J., 2000. Isostatic response of the Australian lithosphere: estimation of effective elastic thickness and anisotropy using multitaper spectral analysis, *J. geophys. Res.,* **105**(8), 19 163–19 184.

Sipkin, S., 1982. Estimation of earthquake source parameters by the inversion of waveform data: Synthetic waveforms, *Physics of the Earth and Planetary Interiors,* **30**(2–3), 242–259.

Sipkin, S., 1986a. Estimation of earthquake source parameters by the inversion of waveform data: Global seismicity, 1981–1983, *Bull. seism. Soc. Amer,* **76**(6), 1515–1541.

Sipkin, S., 1986b. Interpretation of non-double-couple earthquake mechanisms derived from moment tensor inversion *J. Geophys. Res.,* **91**(1), 531–547.

Suvorov, V., Mishenkina, Z., Gennadii, V., Sheludko, I., Selenzev, V. & Solovyov, V., 2002. Structure of the crust in the Baikal rift zone and adjacent areas from deep seismic sounding data, *Tectonophysics,* **351,** 61–74.

Taylor, L., Snyder, G., Keller, R., Remley, D., Anand, M., Wiesli, R., Valley, J. & Sobolev, N., 2003. Petrogenesis of group A eclogites and websterites: evidence from the Obnazhennaya kimberlite, Yakutia, *Contrib. Mineral. Petrol.,* **145,** 424–443, doi:10.1007/s00410-003-0465-y.

Taymaz, T., Jackson, J. & Westaway, R., 1990. Earthquake mechanisms in the Hellenic trench near Crete, *Geophys. J. Int.,* **102,** 695–731.

ten Brink, U. & Taylor, M., 2002. Crustal structure of central Lake Baikal: insights into intracontinental rifting, *J. geophys. Res.,* **107**(7), 2132, doi:10.1029/2001JB000300.

van der Beek, P., 1997. Flank uplift and topography at the central Baikal rift (SE Siberia): a test of kinematic models for continental extension, *Tectonics,* **16**(1), 122–136.

Vertlib, M., 1981. Determination of focal depths by the composite method for some regions of Pribaikalie, in *Seismic investigations in East Siberia,* pp. 82–88, ed. Rogozhina, V., Nauka, Moscow, (in Russian).

Vertlib, M., 1997. Hypocentral field and mechanism of earthquakes in relation to geodynamics of the northeastern Baikal zone, *Geologiya i Geofizika (Russian Geology and Geophysics),* **37**(8), 1414–1422.

Wessel, P. & Smith, W., 1998. New, improved version of Generic Mapping Tools released, *EOS, Trans. Am. geophys. Un.,* **79**(47), 579.

Wiens, D. & Stein, S., 1983. Age dependence of oceanic intraplate seismicity and implications for lithospheric evolution, *J. geophys. Res.,* **88**(8), 6455–6468.

Xu, Y., Shankland, T., Linhardt, S., Rubie, D., Langenhorst, F. & Klasinski, K., 2004. Thermal diffusivity and conductivity of olivine, wadsleyite and ringwoodite to 20 GPa and 1373 K, *Phys. Earth planet. Inter.,* **143,** 321–336, doi:10.1016/j.pepi.2004.03.005.

Zorin, Y., Mordvinova, V., Turutanov, E., Belichenko, B., Artemyev, A., Kosarev, G. & Gao, S., 2002. Low seismic velocity layers in the Earth's crust beneath Siberia (Russia) and Central Mongolia: receiver function data and their possible geological implication, *Tectonophysics,* **359,** 307–327.

Zwick, P., McCaffrey, R. & Abers, G., 1994. MT5 program, *IASPEI Software Library,* **4**.

APPENDIX A: WAVEFORM INVERSION FOR ALL SOURCE PARAMETERS

Here we present the *P* and *SH* long-period waveforms (Figs A1–A13) for the events labelled 'A' in Table 1. We have inverted these waveforms for source orientation, depth and moment. Using a deconvolution procedure, we produced long-period records from broadband data by switching the response of a GDSN broadband instrument for that of a digital WWSSN 15–100 long-period seismometer. Wherever possible, arrival times of *P* and *SH* phases were measured from the broadband records and used to realign the long-period synthetics with the observed waveforms, before performing the inversion. We used the MT5 version (Zwick et al., 1994) of the algorithm developed by McCaffrey & Abers (1988) and McCaffrey *et al.* (1991), which inverts *P* and *SH* waveform data for the source time function (parametrised by a series of overlapping isosceles triangles), scalar moment, strike, dip, rake, and centroid depth. *P*, *pP*, and *sP* phases were modelled on vertical component seismograms in the epicentral distance range 30–90º, and the *S* and *sS* phases on transverse components in the range 30–80º. Each source was constrained to be a pure double-couple and amplitudes were corrected for geometrical spreading. Anelastic attenuation was modelled using Futterman operators with a t^* of 1.0 and 4.0 s for *P* and *SH* waves respectively. We estimated the uncertainty in our source depth by fixing it at some value close to that of the best fitting ("minimum misfit") solution, before varying the other source parameters to compensate for this change. The range of acceptable depths was taken to be that outside which the inversion could not adequately match the waveforms through adjustment of the remaining free parameters.

Each figure is divided into two parts: (*a*) The minimum misfit solution, showing focal spheres for *P* (top circle) and *SH* (bottom circle) waves as lower hemisphere projections. Pressure and tension axes are shown in the *P* focal sphere as solid and open circles respectively. Below the event label we list the strike, dip, and rake for one of the nodal planes (s1, d1, r1, Table 1), the centroid depth in km, and the seismic scalar moment in Nm. Each waveform is labelled by its station code and an additional letter. These letters are ordered clockwise by azimuth and correspond to the event-station raypath's intersection with the lower hemisphere. Vertical bars and numbers beside each focal sphere denote the amplitudes (in microns) of the plotted seismograms. For the waveforms themselves, solid lines show the observed seismograms; dashed lines show synthetics calculated for the minimum misfit solution. The inversion window is marked by vertical bars at either end of each waveform. To the right of each P focal sphere, the horizontal timescale for both sets of waveforms is shown along with the source time function. (*b*) We show the sensitivity of the minimum misfit solution to variations in source depth. The effects of changes in source parameters are shown for six good quality waveforms (three *P*, three *SH*), selected from as wide a range of azimuths as possible. Line (*i*) shows
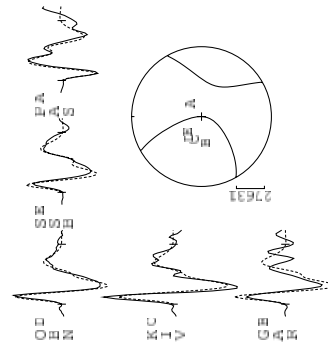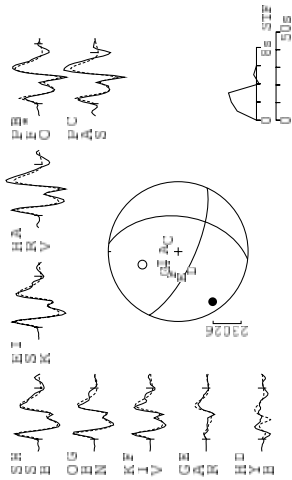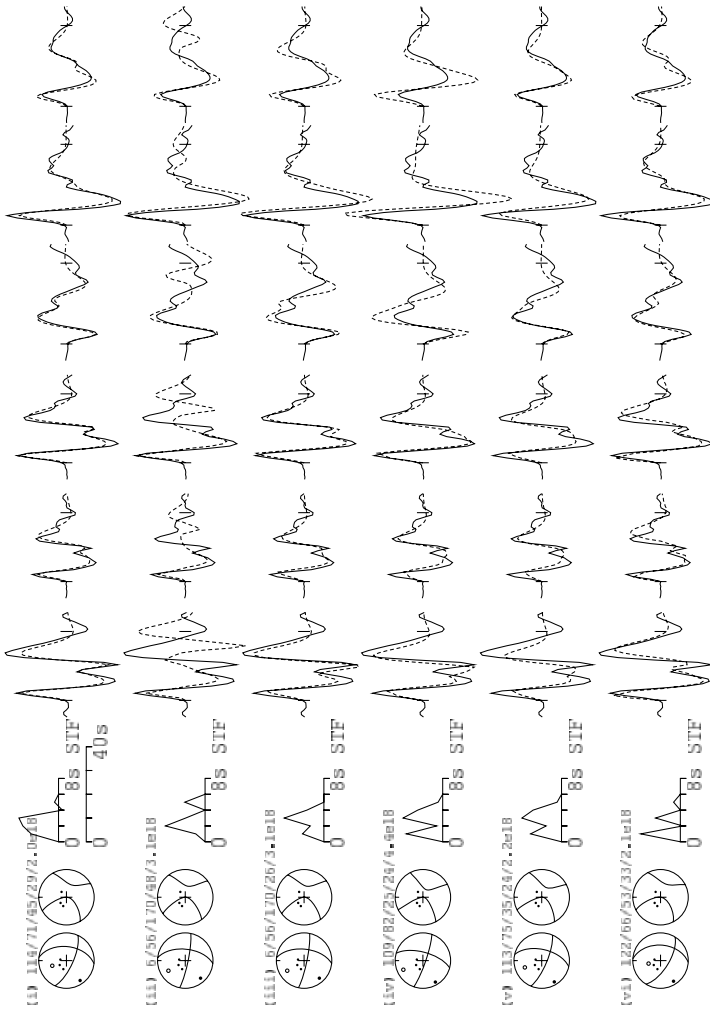
Figure A1. 1989 April 20 (890420). (*a*) Minimum misfit solution: strike 114°; dip 71°; rake 45°; depth 29 km; M_w 6.2. We halved the gain for the *P* record at PFO (indicated by *) and, consequently, did not use it in the inversion. (*b*) Sensitivity analysis: (*i*) Minimum misfit solution shown in (*a*); (*ii*) Harvard CMT solution, with a centroid depth of 45 km. The synthetics are clearly too broad at all stations shown; (*iii*) Harvard CMT source orientation and moment, but with the depth fixed at the EHB value of 26 km. Synthetics are slightly too narrow at HRV(*P*) and PAS(*SH*); (*iv*) The solution of Doser (1991b), using a moment corresponding to M_w 6.4. Synthetics are again too narrow at HRV(*P*) and PAS(*SH*), and are most notably too large in amplitude for the *SH* waves; (*v*) Depth fixed at 24 km. The synthetics are too narrow at HRV(*P*) and PAS(*SH*); (*vi*) Depth fixed at 33 km. The synthetics are too broad, shown most clearly at stations KIV(*P*) and ESK(*P*). Event depth 29^{+4}_{-5} km.
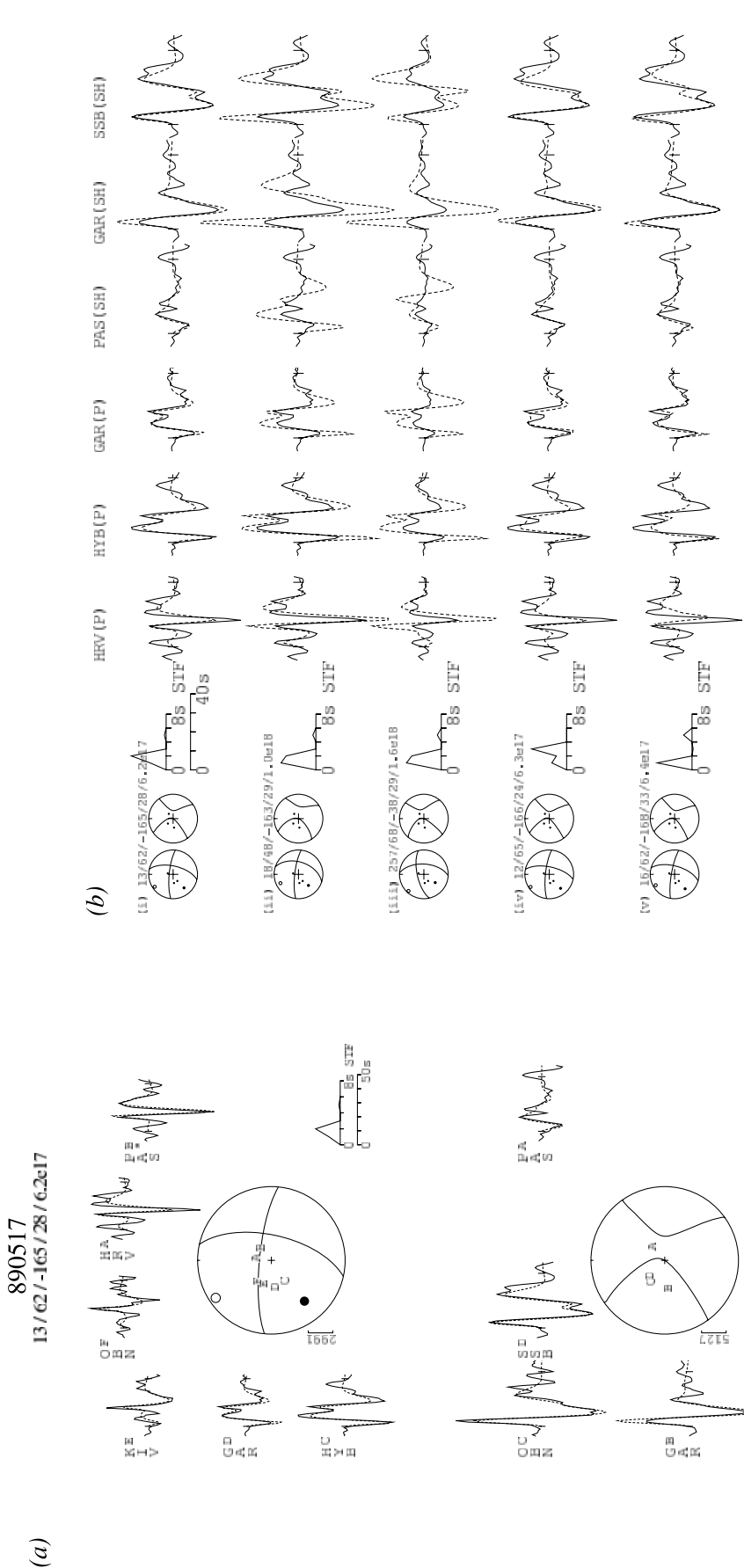
Figure A2. 1989 May 17 (890517). (*a*) Minimum misfit solution: strike 13°, dip 62°, rake −165°; depth 28 km; M_w 5.8. As with event 890429 (Fig. A1), we halved the gain for the *P* record at at station PAS (indicated by *) and, consequently, did not use it in the inversion. (*b*) Sensitivity analysis: (*i*) Minimum misfit solution shown in (*a*); (*ii*) Harvard CMT solution. The Harvard centroid depth of 29 km is similar to the EHB depth (31 km) for this event. The fits to the waveform shapes are of a comparable quality to the those in the minimum misfit solution, but the Harvard scalar moment produces synthetic amplitudes that are too big; (*iii*) The solution of Doser (1991b), using a moment corresponding to M_w 6.1, plotted at half the magnification of the other plots. As with the Harvard solution, the fits to the waveform shapes are of a comparable quality to the those in the minimum misfit solution, but the scalar moment produces amplitudes that are too big; (*iv*) Depth fixed at 24 km. The synthetic waveforms are not wide enough to match the peaks at HYB(*P*), HYB(*P*) and SSB(*SH*); (*v*) Depth fixed at 33 km. The fit is notably degraded at stations HRV(*P*), HYB(*P*) and SSB(*SH*). Event depth 28^{+5}_{-4} km.

Figure A3. 1994 April 26 (940426). (*a*) Minimum misfit solution: strike 81°; dip 24°; rake −56°; depth 14 km; M_w 5.4. (*b*) Sensitivity analysis: (*i*) Minimum misfit solution shown in (*a*); (*ii*) Harvard CMT solution, with a centroid depth of 17 km. The synthetics are too broad, most noticeably for the *P* records; (*iii*) The Harvard CMT source orientation and moment, with the depth fixed at the EHB value of 14 km. There is negligible difference between this model and the minimum misfit solution; (*iv*) Depth fixed at 10 km. The inversion lengthens the source time function in an attempt to fit the width of the seismograms, but the initial double pulse that was well fitted at OBN(*P*) is not reproduced; (*v*) Depth fixed at 18 km. The *P* synthetics are clearly too broad and the shape at HYB(*SH*) is degraded. Event depth 14^{+4}_{-4} km.
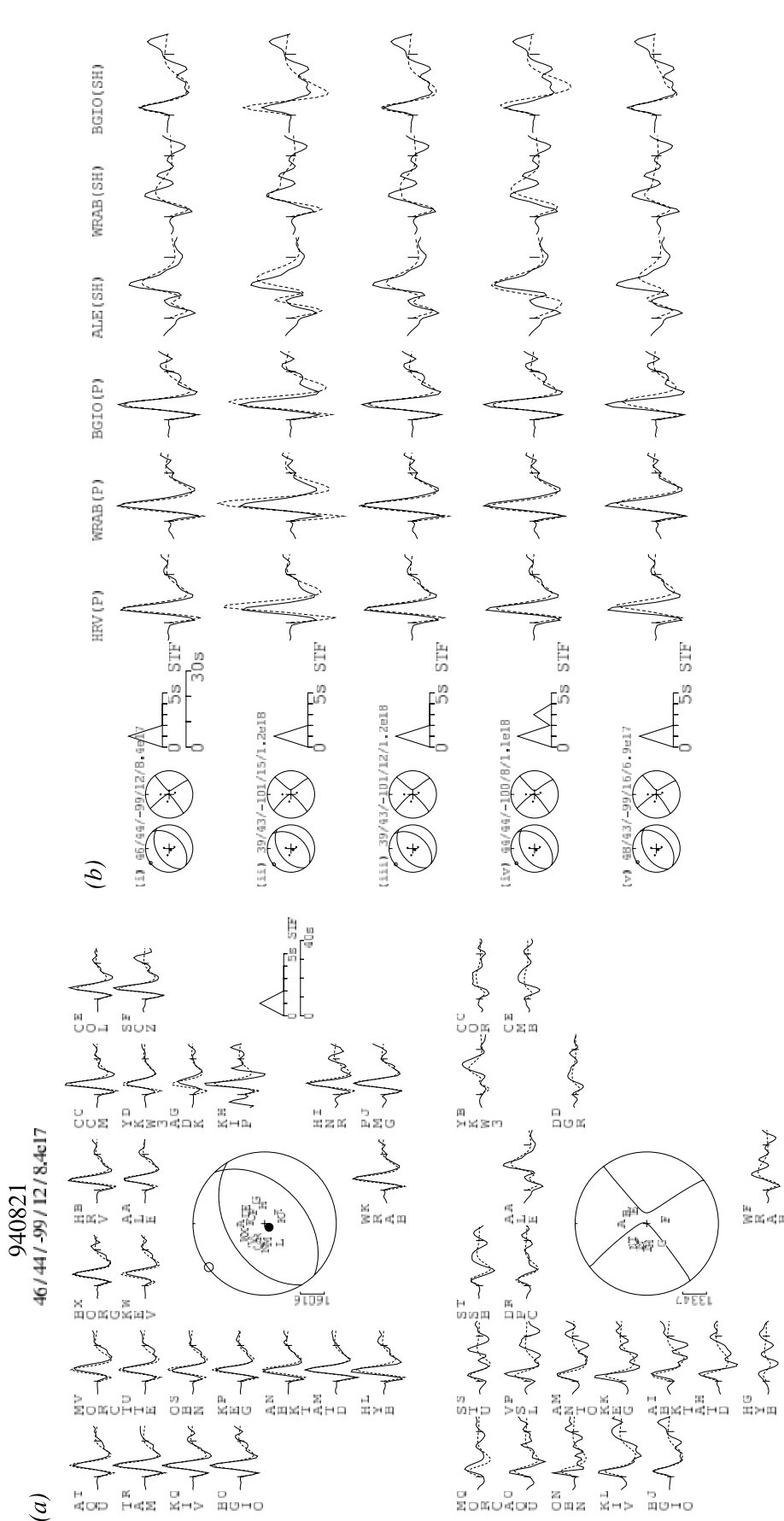
Figure A4. 1994 August 21 (940821). (*a*) Minimum misfit solution: strike 46°; dip 44°; rake −99°; depth 12 km; M_w 5.9. (*b*) Sensitivity analysis: (*i*) Minimum misfit solution shown in (*a*); (*ii*) Harvard CMT solution, with a centroid depth of 15 km. The synthetics are too broad, most notably for the *P* records; (*iii*) Harvard CMT source orientation and moment, with the EHB depth of 12 km, showing negligible difference from our minimum misfit solution; (*iv*) Depth fixed at 8 km. The inversion partly compensates for a shallower depth by increasing both the source time function duration and event magnitude, but does not match the *SH* arrivals at ALE and WRAB by doing so; (*v*) Depth fixed at 16 km. The synthetics are most notably too broad at stations HRV(*P*) and BGIO(*P*). Event depth 12^{+4}_{-4} km.
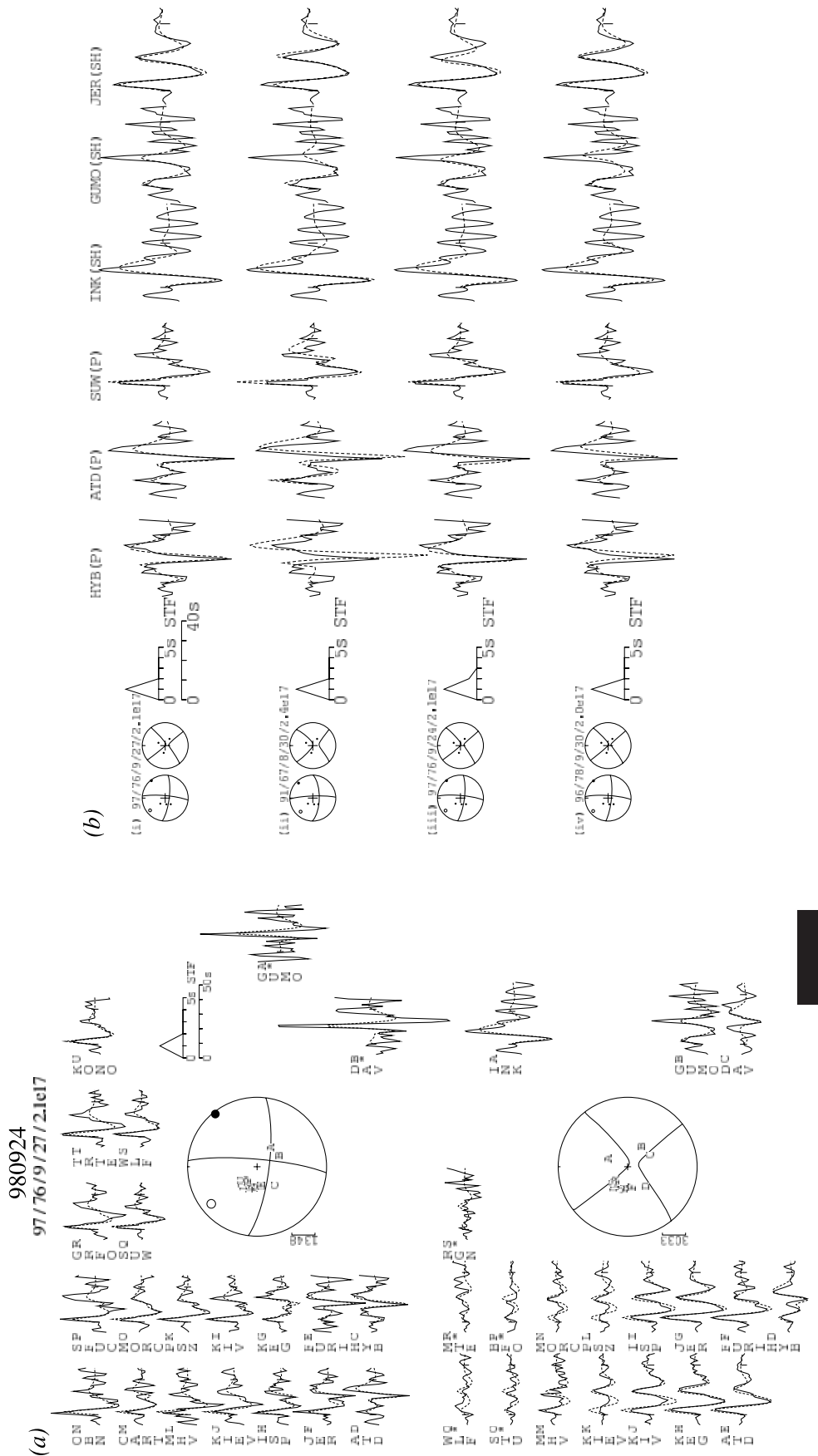
Figure A5. 1995 June 29 (950626). (*a*) Minimum misfit solution: strike 73°; dip 41°; rake −40°; depth 16 km; M_w 5.7. (*b*) Sensitivity analysis: (*i*) Minimum misfit solution shown in (*a*); (*ii*) Harvard CMT solution, with a fixed centroid depth of 15 km. The amplitude is overestimated at all six stations shown here; (*iii*) The fit is not improved by using the Harvard CMT source orientation and moment, with the EHB depth of 16 km; (*iv*) The solution of Bayasgalan et al., (2005), which has a source orientation that is notably different from both ours and that of the Harvard CMT. The fit to ESK(*P*) is notably poor; (*v*) Depth fixed at 10 km. The inversion is able to match most of the features in the data by lengthening the source time function, separating it into two pulses. However, the fit at the *SH* stations PMG and SSB has worsened; (*vi*) Depth fixed at 21 km. Despite shortening the source time function, the synthetics for the *SH* records provide a poorer fit to the data. Event depth 16^{+5}_{-6} km.

Figure A6. 1998 September 24 (980924). (*a*) Minimum misfit sol[...]97°; dip 76°; rake 9°; depth 27 km; M_w 5.5. Stations marked * are not included in the inversion, either because they may have an [...]

(c)

G: OEN

F: KIV

A: BILL

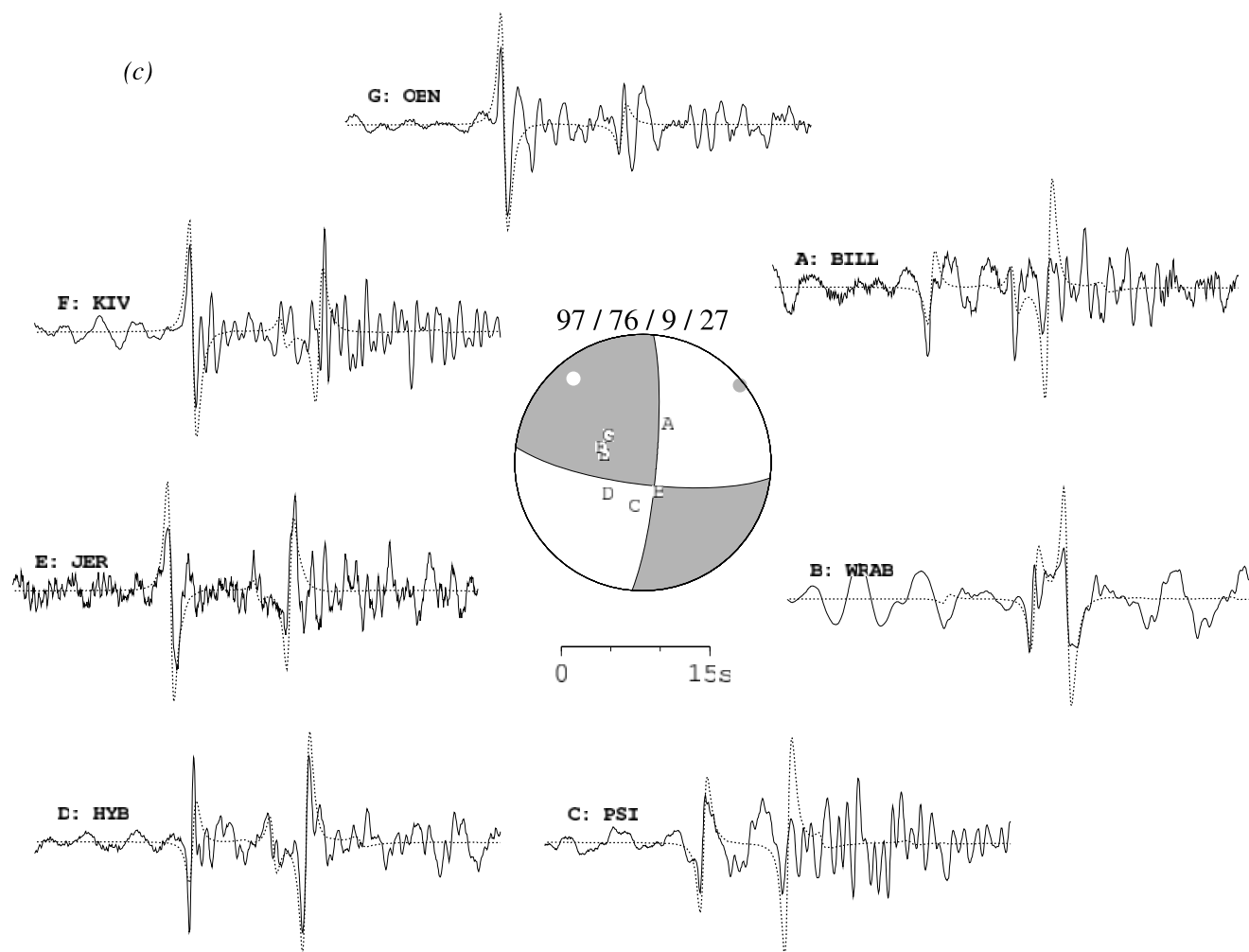97 / 76 / 9 / 27

E: JER

B: WRAB

0   15s

D: HYB

C: PSI

Figure A6. (Continued).

the minimum misfit solution for these six stations. Remaining lines show the effect of using other source orientations and depths. We compared our solution to that of the Harvard CMT catalogue, and also modelled depths published in the updated catalogue of Engdahl *et al.*, (1998, referred to as EHB). We also compared our solution with other published ones where available. The source time function used in all such comparisons is that which minimised the misfit to the data, using the same number of elements as we did in our own solution. Finally, we performed depth sensitivity tests by fixing the depth and observing the inversion's ability to match the waveforms by varying the other source parameters.

APPENDIX B: LONG-PERIOD AND BROADBAND MODELLING OF SOURCE DEPTHS

In this appendix we present waveform modelling results (Figs A14–A18) for the five events labelled 'A' in Table 2. For two of these events (910912 and 920214, Figs A15 and A16), we followed the method described in appendix A1, but fixed the source orientation to that in the Harvard CMT catalogue. Long-period waveforms were then inverted for the source depth and moment, with the source time function restricted to a single element of suitable duration. Depth sensitivity tests were performed for these two events using

the method of appendix A1 and are presented in a similar way. We performed the same procedure for event 050427 (Fig. A18), but made adjustments to the Harvard quick CMT solution before inverting for the depth and moment.

As event 891025 (Fig. A14) had only a single station suitable for long-period waveform analysis, we supported the depth estimated from our long-period depth and moment inversion with a forward model of the broadband vertical-component waveform. We used the program WKBJ3 (Chapman 1978; Chapman *et al.*, 1988) and the Harvard CMT source orientation to do this, as described in section 2.2.2. Broadband forward modelling was also used to match the waveforms at several stations for event 951113 (Fig. A17).

For all WKBJ3-generated synthetic waveforms, the source strike, dip, rake, and modelled depth (in km) are shown above the *P* focal sphere. We do not estimate the scalar moment using this technique. Instead, the rms amplitudes of all synthetic waveforms were scaled to match those in the window of data that we present here. Owing to the presence of noise, this scaling slightly overestimates the absolute amplitudes of the modelled phases. However, we were able to match the *relative* amplitudes and arrival times of the *P*, *pP*, and *sP* phases very well. Station labels within the focal sphere are ordered clockwise by azimuth, as in appendix A1. A timescale for the synthetic (dashed lines) and observed vertical component waveforms (solid lines) is also shown.
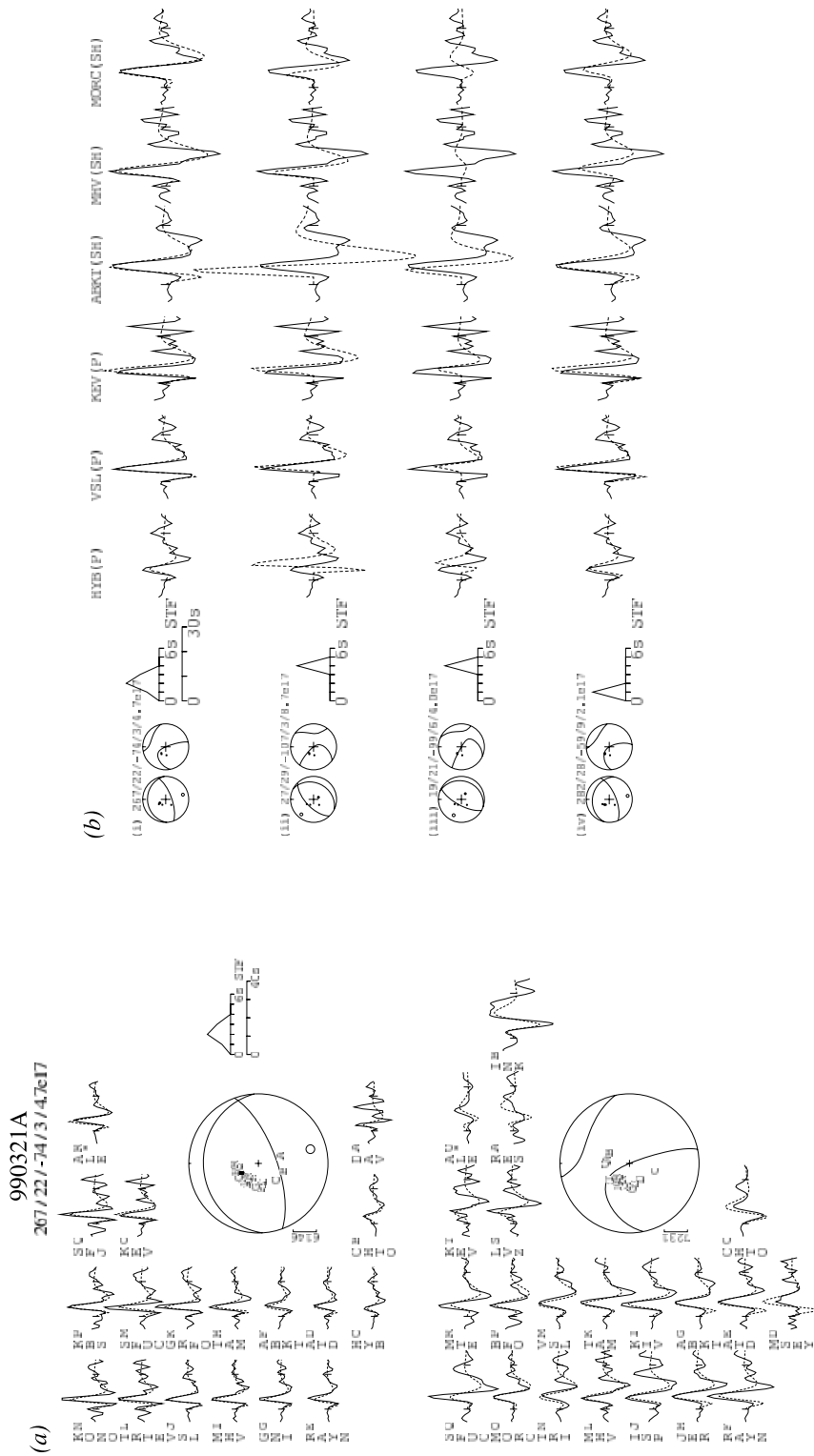
Figure A7. 1999 March 21 (990321A). (*a*) Minimum misfit solution: strike 267°; dip 22°; rake −74°; depth 3 km; M_w 5.7. We halved the gain for both *P* and *SH* records at ALE (indicated by *) and, consequently, did not use them in the inversion. (*b*) Sensitivity analysis: (*i*) Minimum misfit solution shown in (*a*); (*ii*) Harvard CMT source orientation and moment, with the EHB catalogue depth of 3 km. The full Harvard CMT solution, which uses a fixed depth of 15 km, produces an even worse fit than that shown here. Our minimum misfit source orientation differs significantly from that of the CMT solution. The CMT solution is likely to have been affected by event 990321B (M_w 5.8, Fig. A8), which occured around one minute after this event in approximately the same location; (*iii*) The grid-searched solution of Brazier & Nyblade (2003), which was restricted to have a strike, dip, and rake within 10° of the Harvard CMT values; (*iv*) Depth fixed at 9 km. The synthetics are clearly too broad at stations HYB(*P*), KEV(*P*), MHV(*SH*) and MORC(*SH*). The centroid was most likely between the surface and this depth. Event depth 3^{+6}_{-3} km.
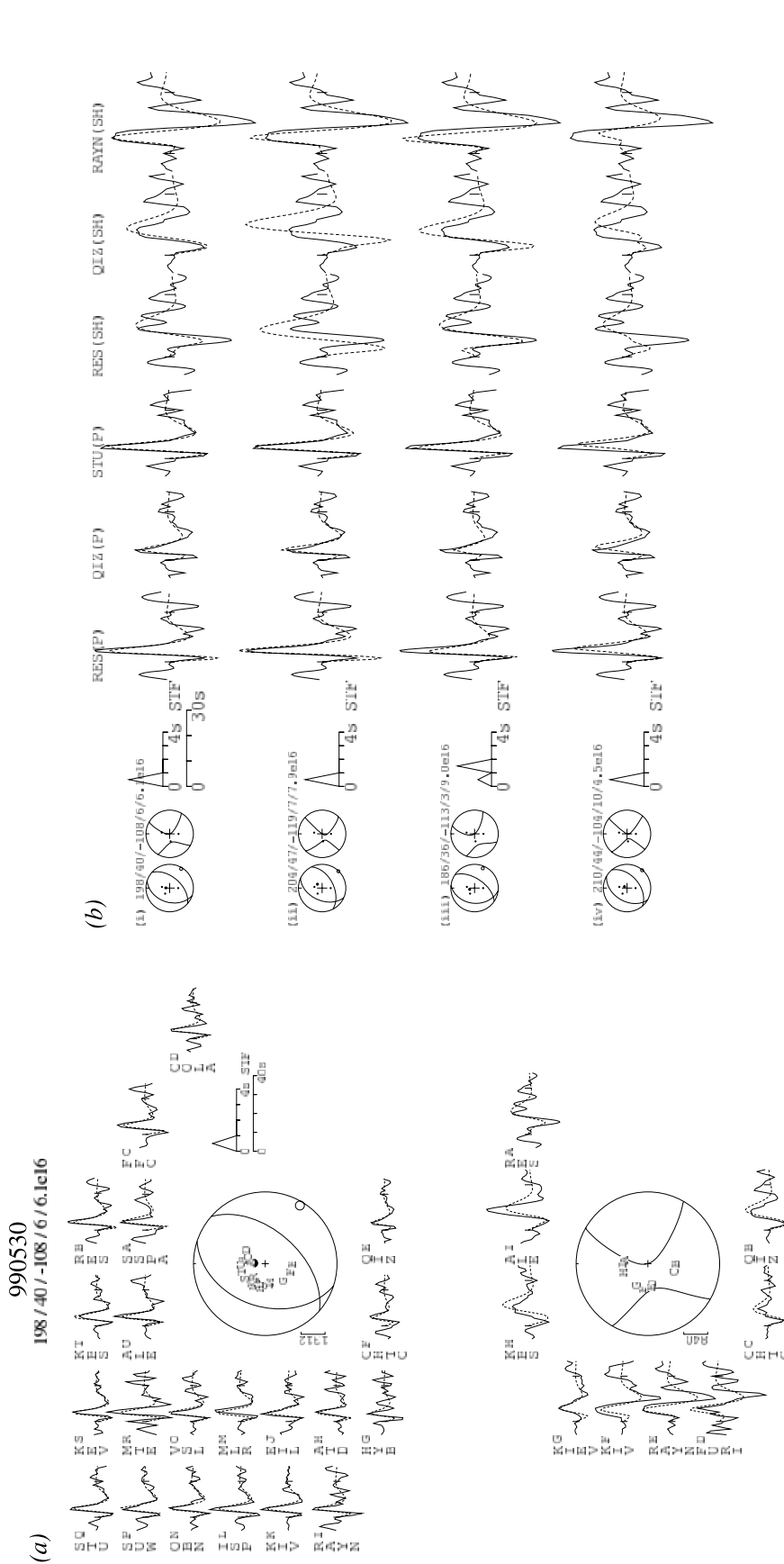
Figure A8. 1999 March 21 (990321B). (*a*) Minimum misfit solution: strike 222°; dip 20°; rake −113°; depth 3 km; M_w 5.8. As with event 990321A (Fig. A7), both *P* and *SH* records at ALE (indicated by *) were not used in the inversion. (*b*) Sensitivity analysis. The Harvard CMT source orientation generally provides a poor fit to the data for a wide range of depths, so instead we have compared our solution with that of the USGS catalogue (Sipkin, 1982, 1986a,b): (*i*) Minimum misfit solution shown in (*a*); (*ii*) USGS solution, with a depth of 9 km. The inversion produced a shorter time function for this set of source parameters, but the synthetics shown are too broad; (*iii*) USGS solution, but using a source depth of 3 km. The fit to the data is much improved relative to (*ii*), though does not fit the *SH* waves as well as the minimum misfit solution; (*iv*) Depth fixed at 7 km. Despite a shorter time function, the *P* synthetic waveforms are too broad and the fit to the *SH* data is clearly degraded. Event depth 3^{+4}_{-3} km.

Figure A9. 1999 May 30 (990530). (*a*) Minimum misfit solution: strike 198°; dip 40°; rake −108°; depth 6 km; M_w 5.2. The data have a surprisingly high signal-to-noise, given the small magnitude of the event. (*b*) Sensitivity analysis: (*i*) Minimum misfit solution shown in (*a*); (*ii*) Harvard CMT source orientation and moment, with the EHB catalogue depth of 7 km. The seismogram widths are still fitted well by this choice of model, but the fit to the amplitude and shape of the *SH* records is worse than that of the minimum misfit solution; (*iii*) Depth fixed at 3 km. Although the inversion is able to partly compensate for the reduction in depth by lengthening the source time function, there is a poorer fit to the amplitudes at several stations; (*iii*) Depth fixed at 10 km. The synthetics are too broad at all stations shown. Event depth 6^{+4}_{-3} km.
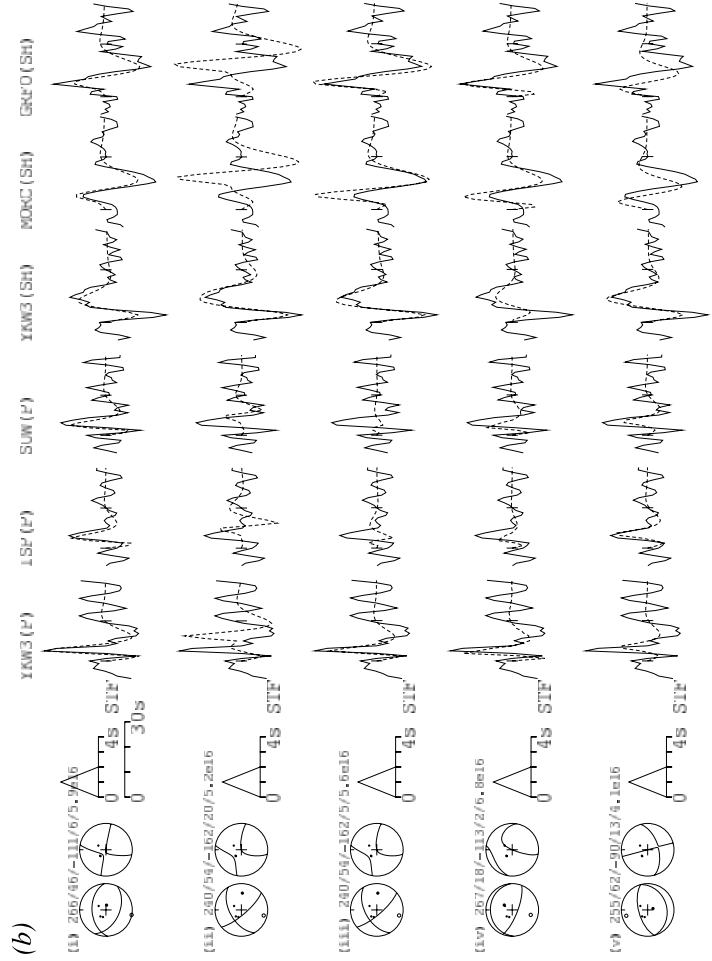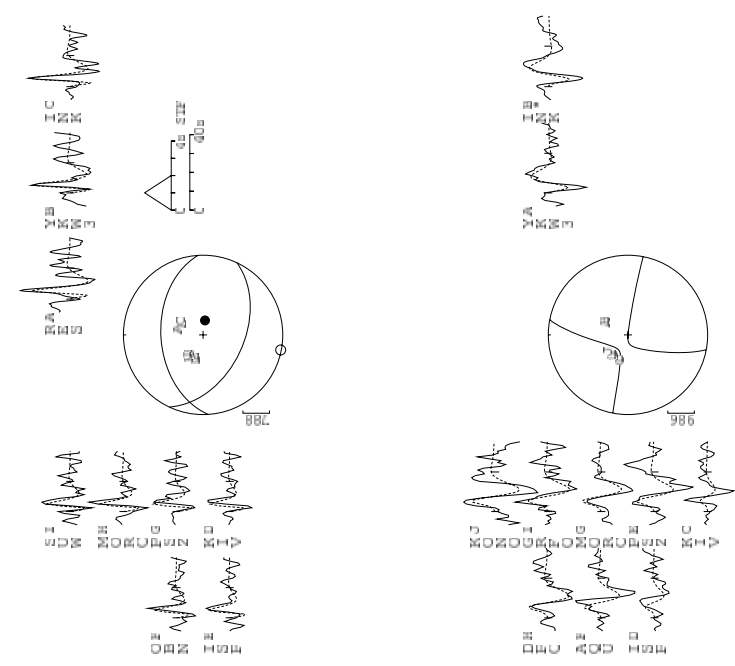
Figure A10. 1999 September 8 (990908). (*a*) Minimum misfit solution: strike 266°; dip 46°; rake −111°; depth 6 km; M_w 5.1. The fit produced by an inversion for and moment only was poor when the source orientation was fixed to that of the Harvard CMT. Because of this, we attempted to invert the data for all source parameters, despite the small event magnitude. However, we restricted the source time function to a single triangular element of 1 s half-duration in all of the analyses presented here. We halved the gain for the *SH* records at INK (indicated by *) and, consequently, did not use that component in the inversion. (*b*) Sensitivity analysis: (*i*) Minimum misfit solution shown in (*a*); (*ii*) Harvard CMT solution, with a depth of 20 km. The EHB depth for this event is 21 km. Clearly the modelled solution is too deep; (*iii*) An inversion for depth and moment using the Harvard source orientation. Although the fit to the *SH* records is comparable to the minimum misfit solution, there is a notably poor fit to the *P* records at ISP and SUW; (*iv*) Depth fixed at 2 km. The *P* waveforms are too narrow and the fit to the *SH* records is clearly much poorer than that of the minimum misfit solution; (*v*) Depth fixed at 13 km. The *P* records are relatively insensitive to an increase in source depth, but their amplitudes are clearly not fitted as well here as they are in the minimum misfit solution. Event depth 6^{+7}_{-4} km.
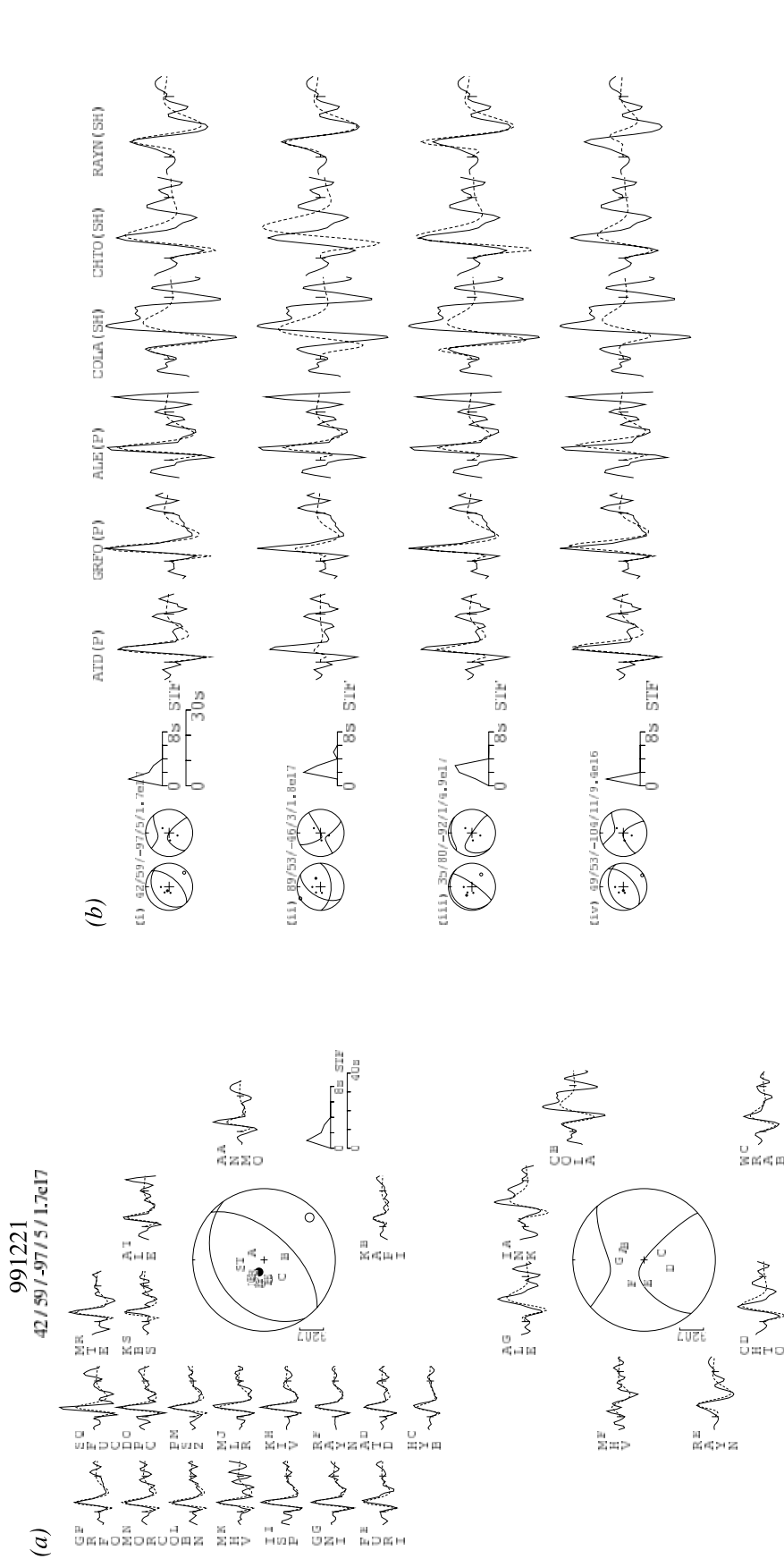
Figure A11. 1999 December 21 (991221). (*a*) Minimum misfit solution: strike 42°; dip 59°; rake −97°; depth 5 km; M_w 5.4. (*b*) Sensitivity analysis: (*i*) Minimum misfit solution shown in (*a*); (*ii*) Harvard CMT source orientation and moment, with the EHB catalogue depth of 3 km. It is apparent from the width of the *P* records that the EHB depth is approximately correct, but the Harvard source orientation poorly fits most of the long period waveforms; (*iii*) Depth fixed at 1 km. The synthetic seismograms are too narrow on the vertical components. Furthermore, the inversion has reoriented the source in an attempt to compensate for the shallow depth, causing the amplitudes of the synthetics to be reduced below the observed values; (*iv*) Depth fixed at 11 km. The synthetics are too broad and the fit to the *SH* waves is poor, most notably at station RAYN. Event depth 5^{+6}_{-4} km.
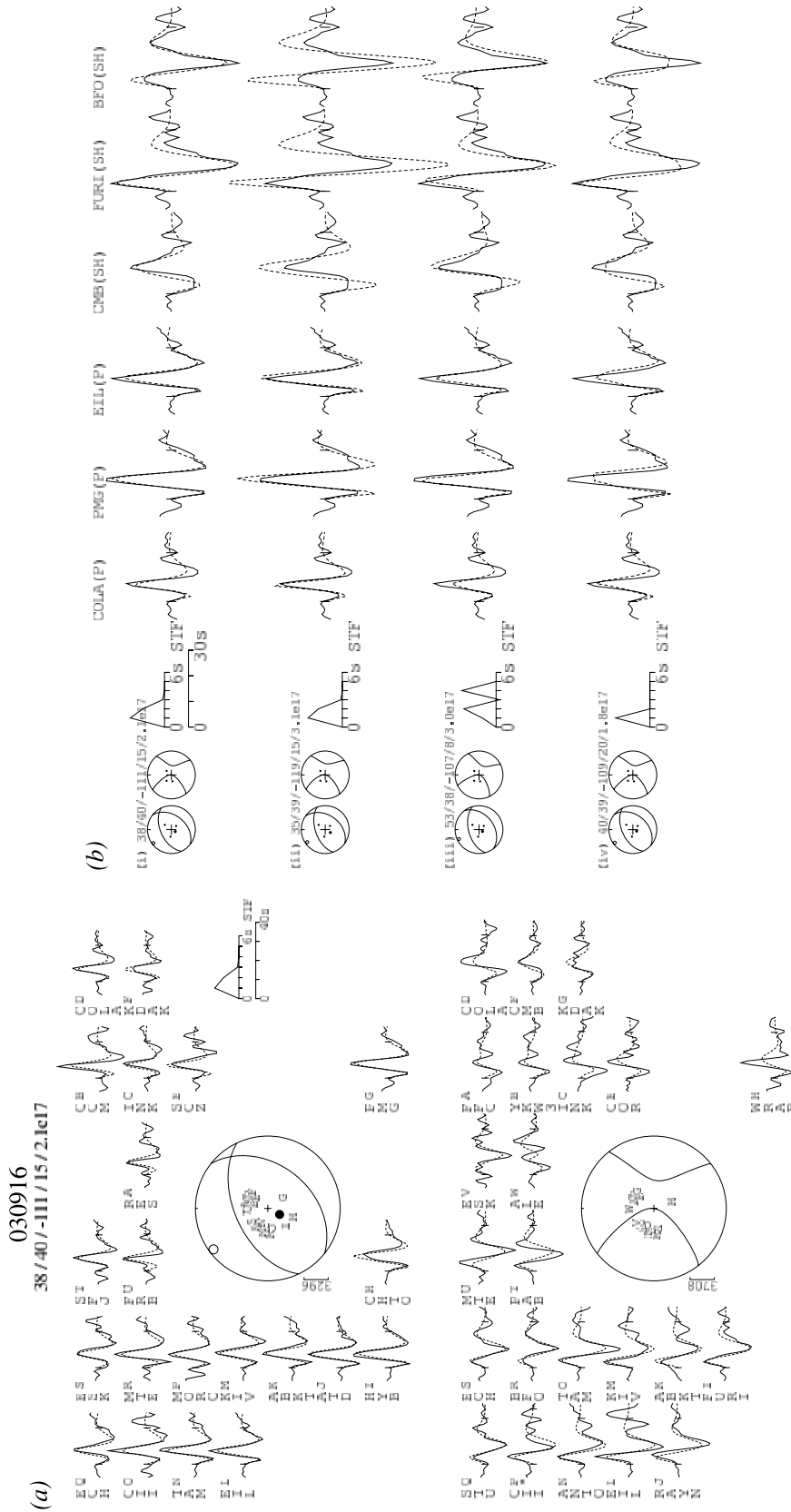
Figure A12. 2003 September 16 (030916). (*a*) Minimum misfit solution: strike 38°; dip 40°; rake −111°; depth 15 km; M_w 5.5. We halved the gain for the *SH* record at CII (indicated by *) and did not use it in the inversion as a result. (*b*) Sensitivity analysis: (*i*) Minimum misfit solution shown in (*a*); (*ii*) Harvard CMT solution, with a fixed depth of 15 km. Synthetics are produced that are similar in shape to those from the minimum misfit solution, but have overestimated amplitudes; (*iii*) Depth fixed at 8 km. The inversion is able to compensate considerably for the shallower depth by lengthening the source time function, but the fit to *SH* records at stations CMB and BFO is worsened by doing this. The fit to the amplitude at COLA(*P*) is also noticeably degraded. (*iv*) Depth fixed at 20 km. The modelled surface reflections at stations PMG(*P*) and CMB(*SH*) have separated from the direct phases. The double peak formed in the synthetics is not seen in the data. Event depth 15^{+5}_{-7} km.
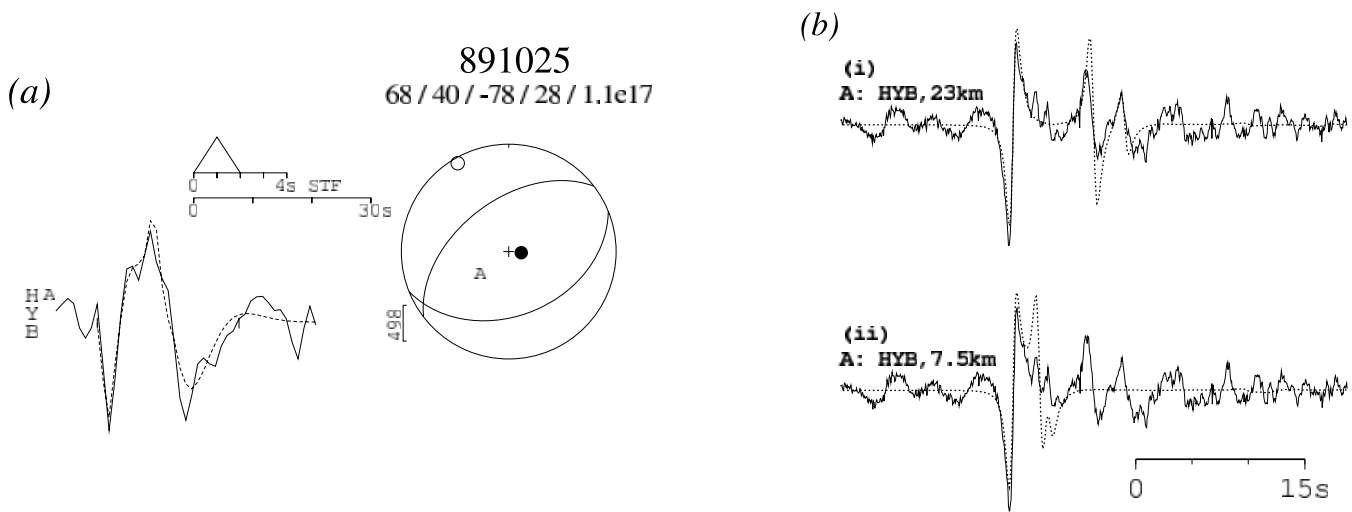
Figure A13. 2005 November 10 (051110). (*a*) Minimum misfit solution: strike 96°; dip 52°; rake −77°; depth 7 km; M_w 5.8. We reduced the gain for *P* and *SH* records at KHC (indicated by *) by a factor of four, and did not use them in the inversion as a result. (*b*) Sensitivity analysis: (*i*) Minimum misfit solution shown in (*a*); (*ii*) Harvard quick CMT solution, with a fixed depth of 12 km. Synthetic seismograms have a similar shape to those in (*a*), but have amplitudes that are slightly too large and the modelled source depth is clearly too deep; (*iii*) Depth fixed at 4 km. The synthetics are noticeably narrower than the observed seismograms; (*iv*) Depth fixed at 11 km. The synthetics are clearly too broad. Event depth 7^{+4}_{-3} km.

Figure A14. 1989 October 25 (891025). (*a*) Results of an inversion for depth and moment only: strike 68°; dip 40°; rake −78°; depth 28 km; M_w 5.3. We used the Harvard CMT source orientation and inverted for the depth and moment only, restricting the source time function to a single element of 1 s half-duration. Although only one station with sufficient signal was available to us, we were able to realign it reliably using the prominent arrival on the broadband vertical component. (*b*) Forward modelling results for the vertical broadband component using the Harvard source orientation. (*i*) A source depth of 23 km reproduces the relative time of the *P*, *pP*, and *sP* phases, and our chosen source orientation matches their relative amplitudes very well; (*ii*) Broadband modelling results for a trial source depth of 7.5 km. We include this model here because it could be argued that the surface reflections *pP* and *sP* arrive within ∼5 s of the *P* phase. Although the polarities of the modelled arrivals match those of arrivals seen in the data, the poorer fit to the relative amplitudes, combined with our findings from the long-period modelling, suggest that the event was not so shallow. We also note a ∼55 s timing error at station HYB on this date. Event depth 28^{+5}_{-5} km.

Two events (990225, 051211) listed in Table 2 have magnitudes which would normally make them suitable for waveform modelling such as that described above. However, we were unable to reliably determine their depths. As discussed in the caption to Table 2, event 990225 (M_w 5.9) had complex waveforms following the onset of the *P* wave, which we were unable to reliably model with a single source or multiple sources. This complexity possibly suggests a complicated rupture history. Radziminovitch *et al.*, (2005) used temporary and permanent stations to relocate 65 aftershocks occurring over three months following the main shock, and found them to be spread from 5–25 km depth, with a mean depth of 15–18 km, depending on the velocity model used for the relocations. Event 051211 (M_w 5.7) occurred a month after event 051110 (M_w 5.8, event depth 7^{+4}_{-3} km, Fig. A13) and was located ∼15 km away. The unusually high level of "noise," presumably the coda from a larger (M_w 6.6) event occurring around an hour and a half earlier in New Britain, prevented us from reliably determining the source depth. Although a similar problem was overcome for event 951113 (M_w

5.8, Fig. A17) using WKBJ3, modelling was not able to unambiguously determine the source depth by applying this technique to broadband data from stations close enough to the event to have sufficient signal-to-noise. Waveforms were consistent with a shallow (∼7 km) focus, but without separation of the *P*, *pP*, and *sP* phases into distinct pulses it was not possible to show this unequivocally.

APPENDIX C: RADIAL RECEIVER FUNCTIONS USED TO INFER CRUSTAL THICKNESSES

In Fig. 8 (main text, section 4) we show a selection of the radial receiver functions that we used to estimate the crustal thickness at three sites (AIKY, CHEY, and YAK) on the Siberian shield. Here, we present all of the receiver function data that we inverted to estimate the Moho depth. Details of the technique we used to estimate a simple crustal structure are given in the main text, along with a discussion of the results.
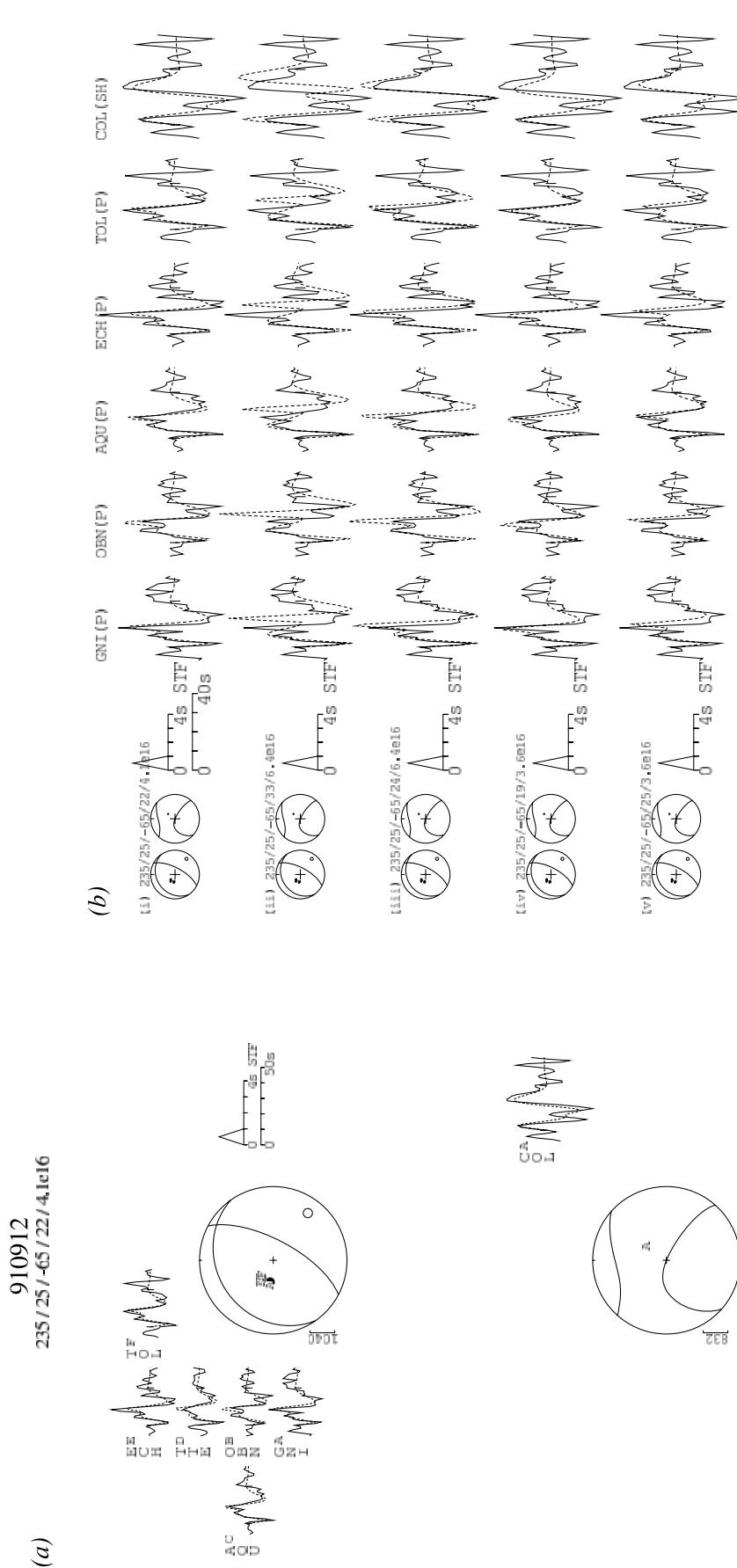
Figure A15. 1991 September 12 (910912). (*a*) Results of an inversion for depth and moment only: strike 235°; dip 25°; rake −65°; depth 22 km; *M*_w 5.0. Stations with sufficient signal on the vertical component plot close to the pressure axis, giving an azimuthal distribution that we could not invert for all source parameters. Instead, we used the Harvard CMT source orientation and inverted for the depth and moment, restricting the source time function to a single element of 1 s half-duration. (*b*) Depth modelling: (*i*) Harvard CMT source orientation, with our best-fitting depth (22 km) and moment, as shown in (*a*); (*ii*) Harvard CMT source orientation, with synthetics that are far too broad; (*iii*) Harvard CMT source orientation and moment, with the EHB depth of 24 km. The Harvard inversion determines the centroid depth to be 33 km, which produces synthetics that are far too broad; (*iii*) Harvard CMT source orientation and moment, with the EHB depth CMT solution (*M*_w 5.2). The Harvard inversion determines the centroid depth to be 33 km, which produces synthetics that are far too broad; (*iii*) Harvard CMT source orientation and moment, with the EHB depth of 24 km. The synthetics fit the width of the data reasonably well, but their amplitudes are overestimated; (*iv*) Depth fixed at 19 km, with the moment free to vary. The peak corresponding to the arrival of the *sP* phase (the *pP* phase is near-nodal) is less well fitted at stations OBN(*P*) and AQU(*P*); (*v*) Depth fixed at 25 km. The arrival of the *sP* phase is clearly too late at GNI(*P*), ECH(*P*), and TOL(*P*). Event depth 22$^{+3}_{-3}$ km.
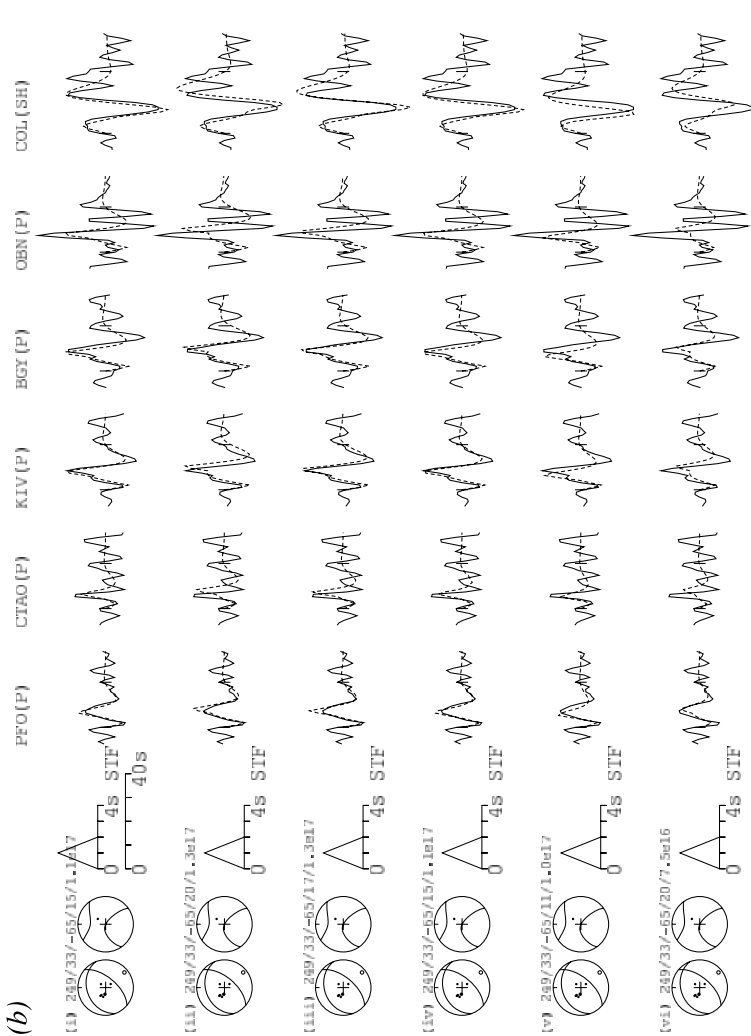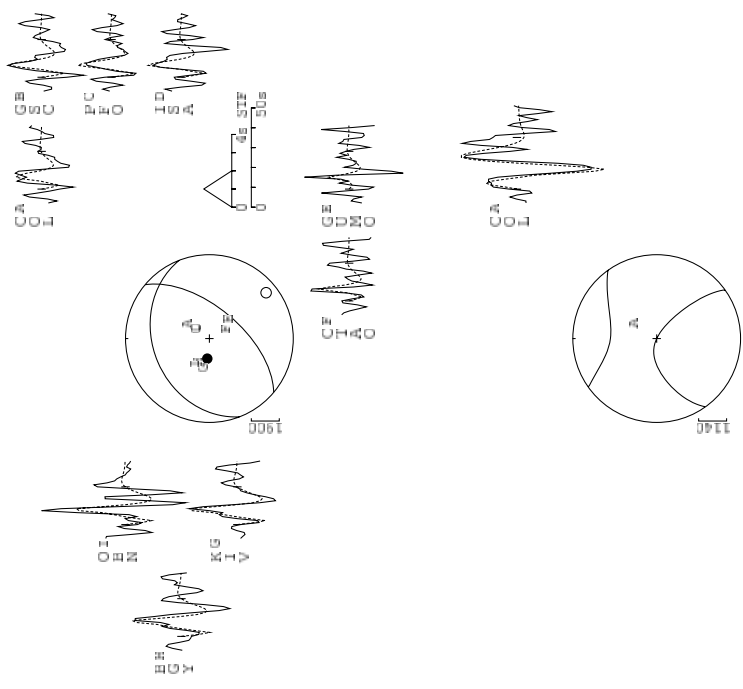
Figure A16. 1992 February 14 (920214). (*a*) Results of an inversion for depth and moment only: strike 249°; dip 33°; rake −65°; depth 15 km; M_w 5.3. The signal-to-noise ratio is poor for this dataset, but we were able to align the onset of the synthetics with picks from the broadband data for several stations. However, the data quality was not sufficient to allow us to invert for all source parameters. As with event 910912 (Fig. A15), we used the Harvard CMT source orientation and inverted for the depth and moment, and restricted the source time function to a single element of 1 s half-duration. As this event was located beneath Lake Baikal, we also investigated the effects of adding a water layer to the surface. (*b*) Depth modelling: (*i*) Harvard CMT source orientation with our best-fitting depth (15 km) and moment, as shown in (*a*); (*ii*) Full Harvard CMT solution (centroid depth 20 km, M_w 5.4). The synthetics are too broad to match the *sP* arrival at stations KIV(*P*) and OBN(*P*), where the *pP* phase is near-nodal; (*iii*) Harvard CMT source orientation and moment, with the EHB depth of 17 km. There is little difference between our final solution and this one, with the exception of a degraded fit at CTAO(*P*) and OBN(*P*); (*iv*) Harvard CMT source orientation, using our best-fitting depth and moment from (*a*), but with a 1 km water layer added above the source. With this choice of source depth and velocity model, the source lies 15 km beneath the free surface (the air-water interface). Inclusion of a 1 km water layer changed the best-fitting depth (as measured from the free surface) by less than 1 km, and had a negligible affect on the best-fitting moment; (*v*) Depth fixed at 11 km (moment free, no water layer); (*vi*) Depth fixed at 20 km (moment free, no water layer). The synthetics are too narrow at KIV(*P*) and BGY(*P*). The synthetics are too broad for several of the *P* records. Event depth 15^{+5}_{-4} km.
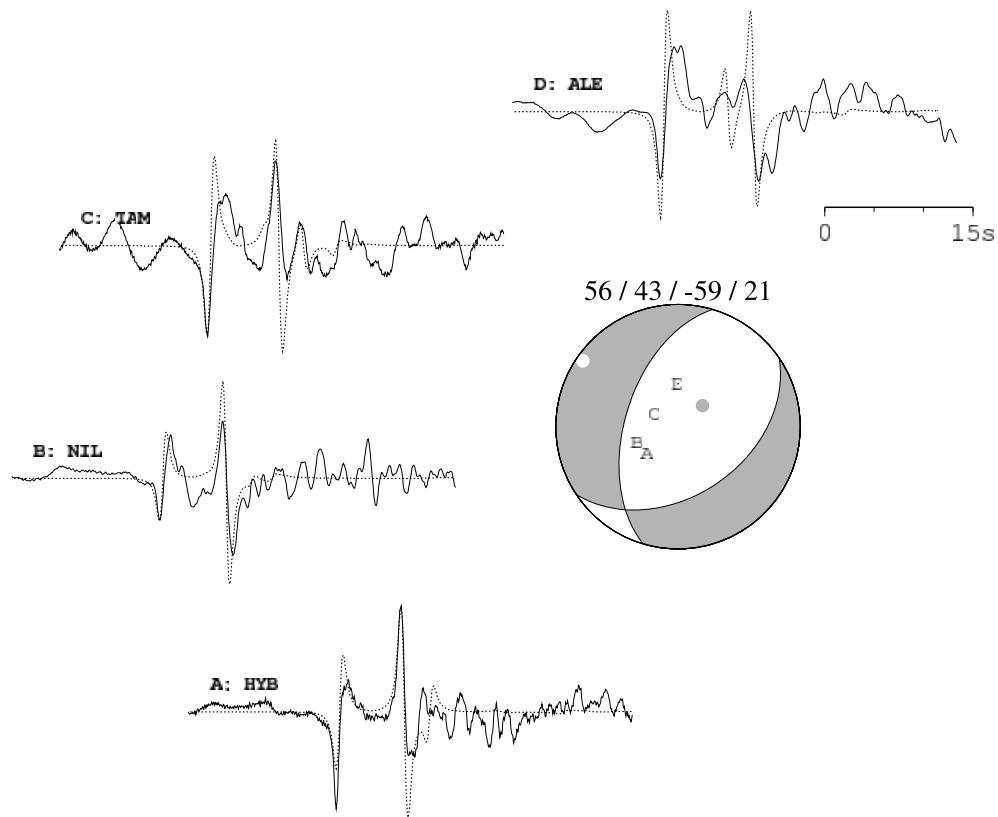
Figure A17. 1995 November 13 (951113). Harvard source orientation with depth determined by forward modelling of vertical component broadband data: strike 56°; dip 43°; rake −59°; depth 21 km; M_w 5.8. Although this event had a magnitude typically suitable for long-period waveform modelling, the coda from a larger (M_w 6.0) Tongan event occurring around an hour earlier made the long-period data too noisy for us to invert. However, the P, pP, and sP phases appear prominently in the broadband records and their relative timing is well matched by the model depth of 21 km shown here. Given the possible inaccuracies in the source velocity model that we use, and the fact that an event of this magnitude is typical of a fault ∼10 km across, we estimate the error in the depth to be ∼5 km. Event depth 21^{+5}_{-5} km.
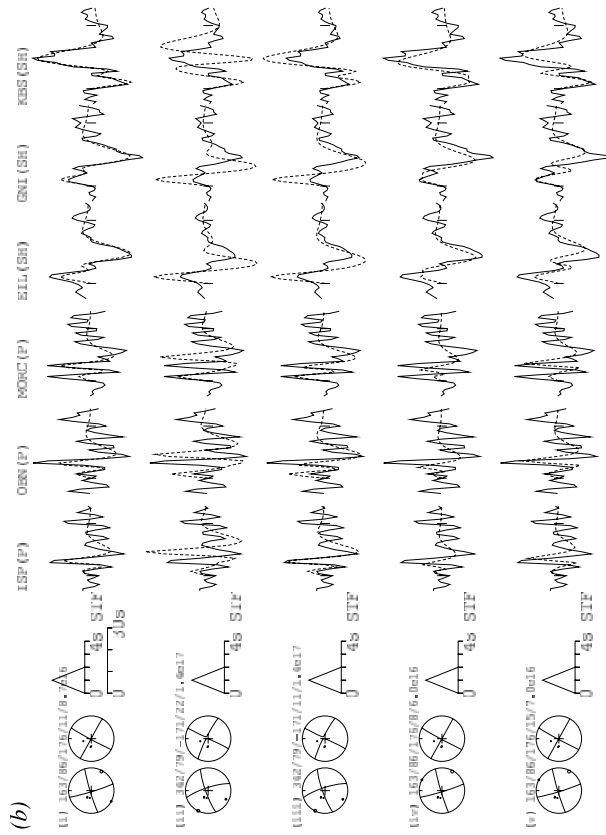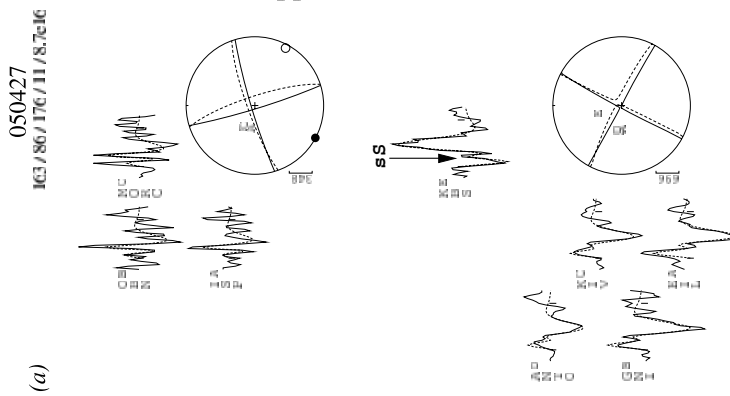
Figure A18. 2005 April 27 (050427). (*a*) An inversion for depth and moment using a fixed strike, dip, and rake that differ slightly from those listed by the Harvard quick CMT catalogue. We restricted the source time function to a single element of 1 s half-duration. The solution shown has strike 163°; dip 86°; rake 176°; depth 11 km; M_w 5.3, but is poorly constrained in orientation owing to the sparse azimuthal coverage provided by stations with sufficient signal. The Harvard quick CMT solution (dashed line, strike 342°; dip 79°; rake −171°; depth 22 km; M_w 5.4) is presented for comparison and it is this source orientation that is shown in Table 2 and Fig. 2. Synthetics are aligned with the data by eye, as the broadband data is too noisy to reliably pick any onset times. Although there is the possibility of misalignment, the clinching piece of evidence for a shallow depth comes from the relative timing of the clearly separated *S* and *sS* phases, seen most prominently at station KBS(*SH*) where it is labelled *sS*. (*b*) Depth modelling: (*i*) The solution shown in (*a*); (*ii*) The full Harvard quick CMT solution, which is clearly too deep; (*iii*) The Harvard quick CMT source orientation and moment, but with a depth of 11 km. The *sS* arrival at station KBS(*SH*) is matched, but this feature is not reproduced at stations EIL(*SH*) and GNI(*SH*), suggesting that corrections to the Harvard source orientation are required; (*iv*) The orientation from (*a*), with the depth fixed at 8 km. There is no longer a clear separation between the synthetic *S* and *sS* phases; (*v*) Depth fixed at 15 km. The synthetics are too broad. [Note: The *SH* records on lines (*ii*) and (*iii*) are plotted at $\frac{2}{3}$ the magnification of those in other lines.] Event depth 11^{+4}_{-3} km.
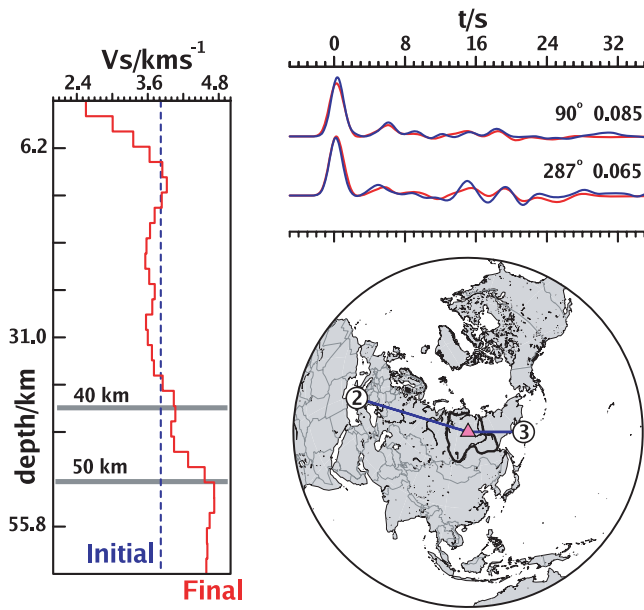
Figure A19. Stacked, true-amplitude radial receiver functions for station AIKY (Fig. 1) and the velocity model (solid red line, left) produced from their inversion. The starting model is a uniform half space of constant V_s=3.82 kms^{-1} (dashed blue line). Synthetic receiver functions produced by the final velocity model shown are plotted in red; stacked data are shown in blue. Numbers by each receiver function give the mean back azimuth and ray parameter (in skm^{-1}) for each stack. The inset map shows the station, the geologically mapped position of the Siberian shield, and the distribution of stacks used in the inversion. Circled numbers indicate the number of events used in each stack. Both stacks used here contain events separated by less than 2.5° of back azimuth and 0.7° of epicentral distance. Primary arrivals and later crustal multiples are reasonably well fitted using the smoothed velocity model shown, which has a crustal thickness between 46–52 km. Based on this and the effect that variations in the initial velocity have on the final Moho depth, we estimate the crustal thickness (t_c) to be between 40–50 km. Grey lines on the velocity model show this range of Moho depths. t_c =45±5 km.
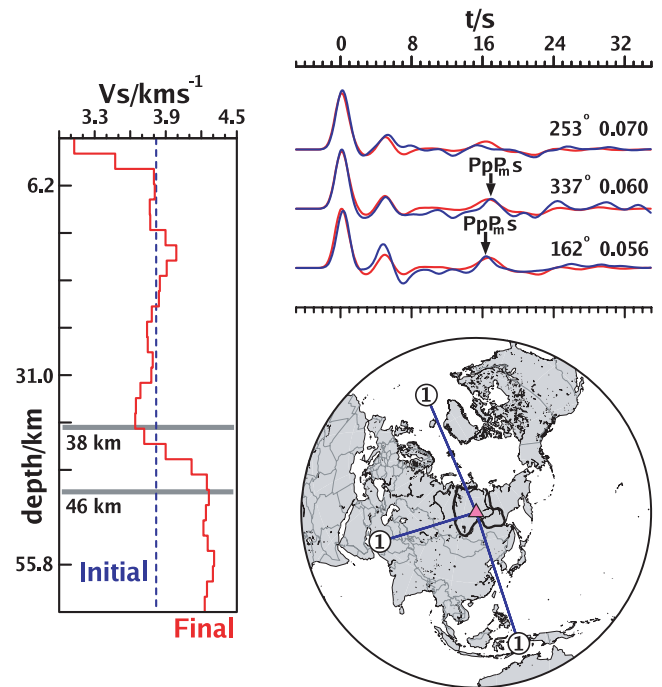

Figure A20. Single event radial receiver functions for station CHEY (Fig. 1), displayed as in Fig. A19. There is insufficient high quality data to stack events from similar back azimuths and epicentral distances. Instead, we jointly invert three single event receiver functions. The PpP_ms crustal multiple is labelled where it is prominent in two of the three records, and is well fitted by the final smoothed model shown. The crustal thickness (t_c) resulting from the starting model shown is 40–44 km and, based on the effect variations in the initial velocity have on the final Moho depth, we estimate t_c to be 42±4 km.
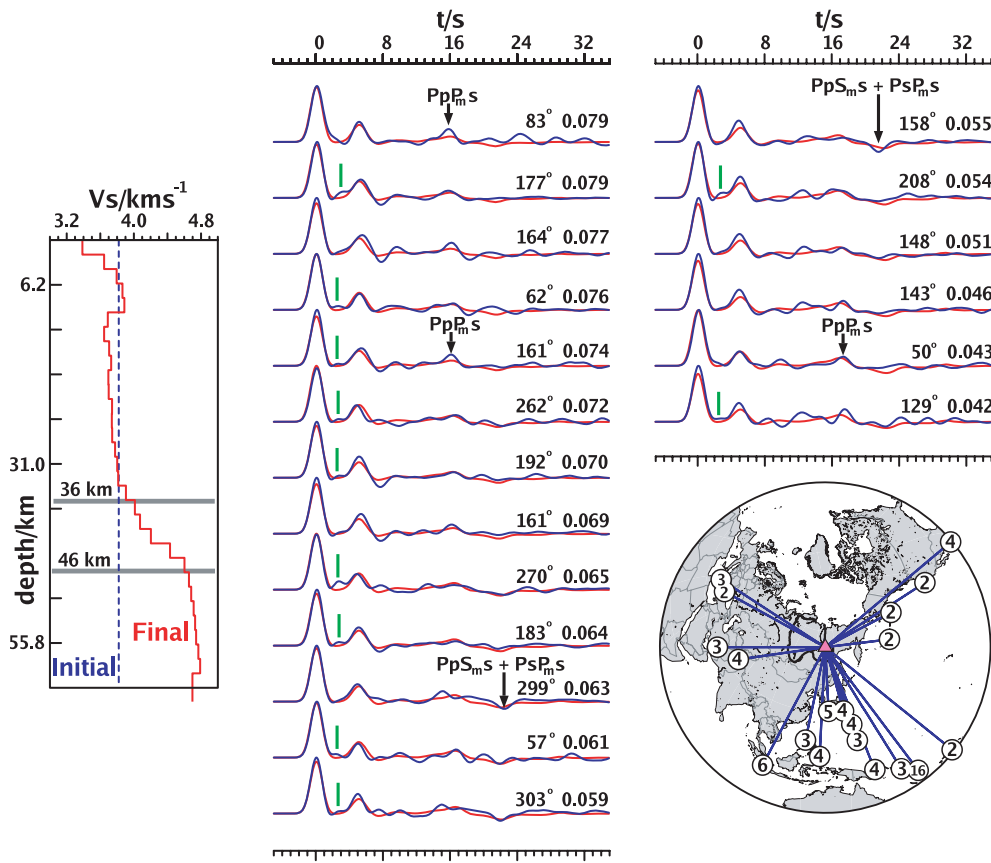
Figure A21. Stacked true-amplitude receiver functions for station YAK (Fig. 1), with prominent crustal multiples PpP_ms and $PpS_ms + PsP_ms$ visible in several of the stacks (examples are labelled). The display convention is as in Fig. A19. An arrival preceding the Ps peak, marked by a vertical green line, is observable in many of the stacks, suggesting that there may be a mid-crustal velocity contrast that is not well resolved by the inversion. Of the 19 stacks presented, 18 use events from a range of back azimuths ($\delta\phi_{baz}$) less than 6°, and 14 have $\delta\phi_{baz}$ <3°. Only one stack uses events from a range of epicentral distances ($\delta\Delta$) exceeding 6°, and 14 stacks have $\delta\Delta$ <2.5°. The Moho of the final smoothed velocity model shown here lies between 36–44 km. t_c =41±5 km.